

Prototype Optical Fiber Mode Scrambler for the
GMT-Consortium Large Earth Finder (G-CLEF)
Spectrograph

Matthew C. H. Leung
Center for Astrophysics | Harvard & Smithsonian
Cambridge, MA, USA

September 2022
Version 1.0

Abstract

When coherent light propagates through a multi-mode optical fiber, the modes interfere at the fiber exit boundary, producing a high contrast speckle interference pattern called modal noise. This non-uniform interference pattern is a problem which particularly affects fiber-fed precision radial velocity (RV) spectrographs, leading to systematic errors and lower signal-to-noise ratios in measurements. To mitigate the effects of modal noise, a device called a fiber mode scrambler is used. A mode scrambler dynamically agitates a fiber, so that the interference pattern will change over time and be smoothed out over long exposures, destroying the modal information in the fiber. This report will discuss about a prototype optical fiber mode scrambler developed for G-CLEF, a precision RV spectrograph which will be one of the first light instruments for the Giant Magellan Telescope. The first part of this project involved redesigning and building a fiber testing setup to image a fiber's near field and far field, and to measure focal ratio degradation. The second part of this project involved designing and building the prototype mode scrambler. Two different mechanical designs for the mode scrambler were tested, along with a variety of fibers, including octagonal, square, and rectangular fibers. The effects of different parameters (e.g. mode scrambler frequency) on mode scrambling were investigated.

Acknowledgements

This internship would not have been possible without the support of many individuals at the CfA. I am deeply grateful to **Dr. Andrew Szentgyorgyi** for the opportunity to work on G-CLEF, for his tireless and persistent efforts in getting me to the CfA, and for his continued support, guidance, and mentorship throughout this project and beyond. I am also very grateful to **Dr. Colby Jurgenson** for his daily mentorship and for teaching me many valuable practical skills in the lab and beyond. I would like to thank **Dr. William Podgorski** and **Mark Mueller** for their guidance and help in the lab. I would also like to express my gratitude to **Dr. Stuart McMuldroch**, **Joseph Zajac**, **Cem Onyuksel**, **Peter Doherty**, and **Daniel Durusky** for their help throughout this project. Finally, I would like to extend my thanks to the administrative staff, especially **Susan Demski-Hamelin** and **Christine Crowley**, who have worked tirelessly to get me to the CfA and to organize my fellowship logistics. Undeniably, this has been by far the best internship I have had, and I would like to thank everyone who has made it amazing. This internship has provided me with an invaluable opportunity to jumpstart a career in astronomical instrumentation, and I hope that one day, I will have a chance to return to the CfA.

Table of Contents

Abstract	i
Acknowledgements	ii
1 Introduction	1
1.1 Preamble	1
1.2 Overview of this Report	2
1.3 Background	2
1.3.1 Two Different Contexts for Fiber Scrambling	2
1.3.1.1 Problem 1: Correlations between Fiber Input and Output .	2
1.3.1.2 Problem 2: Modal Noise	3
1.3.2 In the Context of this Project	4
1.3.3 Fiber Mode Scramblers in the Literature	4
2 FCS: Design	5
2.1 Overview	5
2.1.1 Configuration 1: Through the Fiber	7
2.1.2 Configuration 2: Throughput Measurement	8
2.2 Pre-Injection Arm	9
2.3 Injection Imaging Arm	12
2.4 Near Field Arm	14
2.5 Far Field Arm	15
3 FCS: Assembly and Alignment	17
3.1 Introduction	17
3.2 Tools for Alignment	17
3.2.1 Shearing Interferometer	17
3.2.2 Collimated Source	18
3.2.3 Mini Lab Jack, Vernier Caliper, and Level	18

TABLE OF CONTENTS

3.2.4	Pair of Post-Mounted Irises	19
3.2.5	Pairs of Cage Alignment Plates	19
3.3	Alignment Procedure for Each Arm	19
3.3.1	Pre-Injection Arm	19
3.3.2	Injection Imaging Arm	20
3.3.3	Near Field Arm	22
3.3.4	Far Field Arm	22
3.3.4.1	Initial Approaches	22
3.3.4.2	A More Systematic Approach	23
3.3.4.3	Next Steps	23
3.4	Camera Control Software and Custom Alignment GUI Tools	24
4	Mode Scrambler: Design	27
4.1	Introduction	27
4.2	Mechanical Design	27
4.2.1	Design 1: Simple Rotating Arm	27
4.2.2	Design 2: Four-bar Linkage Crank-Rocker	28
4.3	Electrical and Hardware Design	30
4.3.1	Stepper Motor Drivers	30
4.3.2	Power	31
4.3.3	Electronics Box	31
4.4	Control Software	32
4.4.1	Overview	32
4.4.2	Angular Velocity for Specific Designs	32
4.4.2.1	Design 1: Simple Rotating Arm	32
4.4.2.2	Design 2: Four-bar Linkage Crank-Rocker	33
5	Mode Scrambler: Testing and Analysis	34
5.1	Introduction	34
5.2	Performance the Two Mechanical Designs	34
5.3	Analysis Code	35
5.3.1	Dark, Bias, and Flat Field Correction	35
5.3.2	Fiber Face Boundary Identification	36
5.3.2.1	Ineffective Approaches	36
5.3.2.2	Effective Approach: Overview	37
5.3.2.3	Effective Approach: Detailed Explanation	37
5.3.3	Metric for Mode Scrambling	41

TABLE OF CONTENTS

5.4 Results	41
5.4.1 Example Images	42
5.4.2 Exposure Time and Number of Stacked Frames	43
5.4.2.1 Varying Number of Stacked Frames	44
5.4.2.2 Varying Exposure Time of Individual Frames	45
5.4.2.3 Constant Total Exposure Time	46
5.4.3 Shaft Distance	47
5.4.4 Looping through Several Holes	48
5.4.5 Frequency	49
5.4.5.1 Rectangular Fiber	49
5.4.5.2 Octagonal Fiber	50
6 Conclusion	51
6.1 Summary	51
6.2 Next Steps	52
Bibliography	54

Chapter 1

Introduction

1.1 Preamble

This past year, I had the wonderful opportunity to intern at the Center for Astrophysics | Harvard & Smithsonian (CfA), working under the supervision of Dr. Andrew Szentgyorgyi on the G-CLEF project. G-CLEF (GMT-Consortium Large Earth Finder; [Szentgyorgyi et al. 2018](#)) is a precision radial velocity (RV) echelle spectrograph which will be one of the first light instruments for the Giant Magellan Telescope (GMT). I completed this internship as a part of a co-op/gap year, which is commonly taken by engineering students at my home university, the University of Toronto. From September 2021 to December 2021, I participated in the project remotely as a collaborator, learning the relevant skills and theory, and helping to verify calculations. From January 2022 to June 2022, I worked in-person at the Smithsonian Astrophysical Observatory (SAO) Cambridge Discovery Park (CDP) laboratories, where I learned a lot of practical skills in astronomical instrumentation.

This report will discuss about the project that I worked on within G-CLEF while in-person at SAO CDP, which was a prototype optical fiber mode scrambler for the optical fibers that will feed the spectrograph. The first part of this project involved redesigning and building a fiber testing setup, called the Fiber Characterization Station (FCS), in the Fiber Research Lab at SAO CDP. The second part of the project involved designing and building the prototype mode scrambler.

1.2 Overview of this Report

Section 1.3 provides some background for fiber mode scrambling, and clarifies some confusions in the literature regarding the two different contexts of “fiber scrambling”. Chapter 2 describes the design of the FCS at SAO CDP, which consists of two configurations and four arms. Chapter 3 discusses about the assembly and alignment procedures for the FCS, and about the tools that were developed and used for the alignment process. Chapter 4 discusses about the mechanical, software, and electrical and hardware design of the prototype mode scrambler. Two different mechanical designs were developed and tested. Chapter 5 discusses about the performance of the two prototype mode scrambler designs, the analysis code used to analyze near field images, and the results for the some mode scrambling experiments using the FCS and prototype mode scrambler. Chapter 6 provides a summary of the results of this project and discusses about some next steps.

1.3 Background

1.3.1 Two Different Contexts for Fiber Scrambling

In the literature, there are two different contexts for “fiber scrambling”, for two different problems in multi-mode optical fibers used to feed astronomical spectrographs. The two different contexts are sometimes confused and mixed up in the literature, and will be briefly clarified below. The mode scrambler in this project is intended to address the problem in the second context described below: modal noise.

1.3.1.1 Problem 1: Correlations between Fiber Input and Output

The first problem is that there is some correlation between the distribution of the output light of an optical fiber and the distribution of the input light (Avila et al. 2006; Halverson et al. 2015). This correlation is undesirable. Due to changes in seeing, limitations in the telescope guiding system, and telescope pupil variations, the input of the optical fiber may not be uniformly illuminated and will vary (Sirk et al. 2018; Halverson et al. 2015). Since the fiber output is correlated with the fiber input, the output light distribution will vary as well (Halverson et al. 2015). As a result, the instrument profile will change. That is, there is positional error in the barycenter of the output PSF (Avila et al. 2006). This correlation between the fiber input and output is a significant precision-limiting factor for RV measurements, since the varying fiber output will result in a varying spectrum (Halverson et al. 2015;

Fischer et al. 2016).

In order to reduce the correlation between the input and output, the fiber can be “scrambled” (Ishizuka et al. 2018; Halverson et al. 2015). A “scrambled” output means that the output is independent of the way in which light enters the fiber (Fischer et al. 2016). This is one context for “scrambling”. One popular method to “scramble” the fiber (in this context) is to use an optical “double scrambler”, in which the near field and far field are exchanged using a lens relay (Halverson et al. 2015; Fischer et al. 2016; Sirk et al. 2018). Another name for a “double scrambler” is a “nearfield-farfield exchange coupler” (Ishizuka et al. 2018). Another method is to use fibers with non-circular cross-sections (Fischer et al. 2016), such as an octagonal fiber (Halverson et al. 2015). A device or method which aims to decorrelate the fiber output and input should maximize a metric called the “scrambling gain”, which is the ratio between the displacement of the input light source barycenter and the displacement of the output light source barycenter (Fischer et al. 2016; Avila et al. 2006). This decorrelation is a static correction (Halverson et al. 2015).

1.3.1.2 Problem 2: Modal Noise

The second problem is known as modal noise or speckle noise (Ishizuka et al. 2018; Halverson et al. 2015). An optical fiber is a waveguide, and light propagates through a multi-mode fiber in a finite integer number of electromagnetic modes (Fischer et al. 2016; Petersburg et al. 2018). When coherent light is passed through a multi-mode fiber, the modes interfere at the fiber exit boundary, producing a high contrast speckle interference pattern called modal noise (Halverson et al. 2015; Sablowski et al. 2016; Petersburg et al. 2018). Modal noise severely decreases the signal-to-noise ratio of precision RV spectrographs (Petersburg et al. 2018; Sablowski et al. 2016). The non-uniformity of the interference pattern affects the illumination of the spectrograph, leading to systematic errors (Sirk et al. 2018).

However, if the fiber is moved, then the interference pattern will change because the shape of the waveguide will change. Hence, by mechanically agitating the fiber, the interference pattern will change over time and be smoothed out over long exposures (Petersburg et al. 2018). This technique is also called “scrambling” in this context, in that the modal noise is reduced (Sablowski et al. 2016) and the modal information in the fiber is destroyed (Frank et al. 2018). A device used to mitigate modal noise is called a “fiber mode scrambler” (Ishizuka et al. 2018) or a “fiber agitator” (Sirk et al. 2018). However, unlike the “scrambling” described in Section 1.3.1.1 which is a static correction, the scrambling for modal noise mitigation must be a time-varying correction (Halverson et al. 2015).

1.3.2 In the Context of this Project

The contexts of “scrambling” described in Sections 1.3.1.1 and 1.3.1.2 are different phenomena which have different solutions (Halverson et al. 2015; Sablowski et al. 2016). “Scrambling” in Section 1.3.1.1 refers to scrambling the fiber output from the input, while “scrambling” in Section 1.3.1.2 refers to scrambling the modal information in the fiber. Both phenomena are not the same, but both are detrimental to precision RV measurements. In the context of this project, “scrambling” here will only refer to modal noise mitigation in Section 1.3.1.2. The term “mode scrambler” will be used to emphasize that the modes are being “scrambled”, and not the fiber output from the input.

1.3.3 Fiber Mode Scramblers in the Literature

Most fiber mode scramblers mechanically agitate the fiber in order to mitigate modal noise. However, the generality of mode scramblers in the literature are limited, because they are often specific to a given instrument (Sablowski et al. 2016). Different mode scramblers in the literature mechanically agitate a fiber in different ways, for example by shaking (Frank et al. 2018; Sablowski et al. 2016), bending (Ishizuka et al. 2018), rotating (Petersburg et al. 2018), or twisting (Ishizuka et al. 2018). However, there has not been much research into the best way to agitate a fiber so that the highest amount of modal noise is reduced. My internship project aimed to investigate this.

Chapter 2

Fiber Characterization Station: Design

2.1 Overview

The first part of this project involved redesigning and building a fiber testing setup in the Fiber Research Lab at SAO CDP. This setup is called the Fiber Characterization Station (FCS) and allows for light to be injected into a test fiber. The FCS will test fibers which will be agitated by the mode scrambler prototype. The FCS has four goals, which are to:

1. Image fiber input face (to ensure proper light injection location and alignment)
2. Image fiber near field (fiber output face)
3. Image fiber far field (collimated output of fiber)
4. Measure fiber output power and fiber focal ratio degradation (FRD)

The design of the FCS setup at SAO CDP was inspired by a FCS setup at Yale University ([Petersburg et al. 2018; Tuttle et al. 2020](#)). The FCS design at SAO CDP consists of four arms:

1. Pre-injection arm, to inject light into the fiber
2. Injection imaging arm, to image the fiber input face
3. Near field arm, to image the fiber near field
4. Far field arm, to image the fiber far field

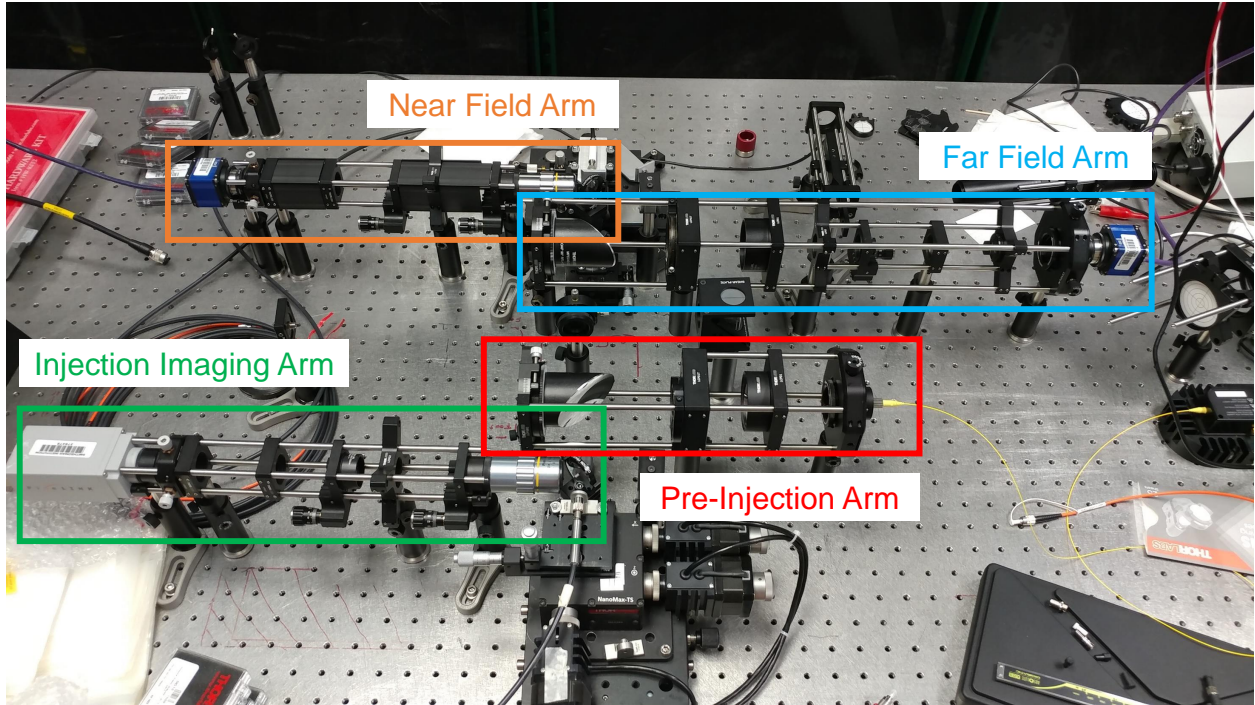


Figure 2.1: Fiber Characterization Station, with the four arms labelled

The FCS is assembled on a floating optical bench. The FCS has two configurations: one in which light is injected through the fiber, and one in which the fiber is bypassed for throughput measurement. An overview of these two configurations, as well as the procedure for FRD measurement, will be discussed in the following two subsections (Sections 2.1.1 and 2.1.2). The remaining sections in this chapter will discuss about the optical and optomechanical design of the FCS' four arms in greater detail.

2.1.1 Configuration 1: Through the Fiber

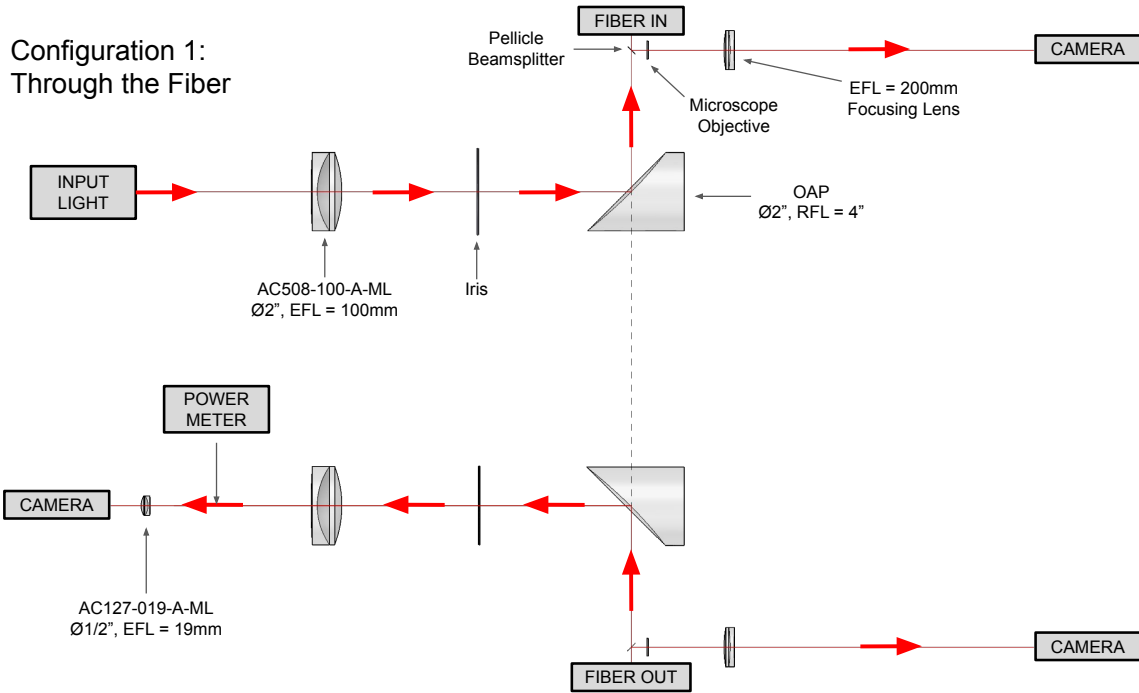


Figure 2.2: Configuration 1 of the FCS. Note that the components are presented here such that this figure is a 180° rotated version of Figure 2.1.

Figure 2.2 shows the first configuration of the FCS. In the first configuration, light is injected through the fiber. Firstly, input light from a certain light source is collimated by an achromatic doublet lens and is then focused by a 90° off-axis parabolic mirror (OAP) onto the input face of the test fiber. Between the lens and the OAP is an iris diaphragm. This is the pre-injection arm. The pre-injection arm basically reimages the input light onto the fiber input face. This reimaging is nearly one-to-one.

Light is also reflected from the fiber input face. This reflected light is then reflected by a pellicle beamsplitter into the injection imaging arm, which is a microscope. After reflection from the pellicle beamsplitter, the light is collimated by an infinite conjugate microscope objective and is then focused by an achromatic doublet lens onto a detector. This arm of the FCS images the fiber input face, to ensure that the light source is correctly injected into the fiber.

The light which is injected into the fiber exits the fiber on the other side of the FCS, which is nearly a mirror copy of the injection side. The output light from the fiber is then split

into two directions by a pellicle beamsplitter. Some of the light is reflected by the pellicle beamsplitter into the near field arm, which is nearly identical to the injection imaging arm. This reflected light is then collimated by an infinite conjugate microscope objective and is then focused by an achromatic doublet lens onto a detector. The near field arm images the output face of the fiber, imaging the near field of the fiber. The only difference between the near field arm and the injection imaging arm is the detector used.

The rest of the light which is not reflected by the pellicle beamsplitter instead passes through the beamsplitter and is collimated by a 90° OAP. The collimated beam is refocused by an achromatic doublet lens. Between the OAP and the lens is an iris diaphragm. At the focus of the lens is a power meter, which is removable. The power meter is used to measure the output power of the fiber, for FRD measurements. If the power meter is not in place, then the focused beam expands and is recollimated by another achromatic doublet lens. The collimated beam then hits a detector, which images the far field of the fiber. This is the far field arm.

2.1.2 Configuration 2: Throughput Measurement

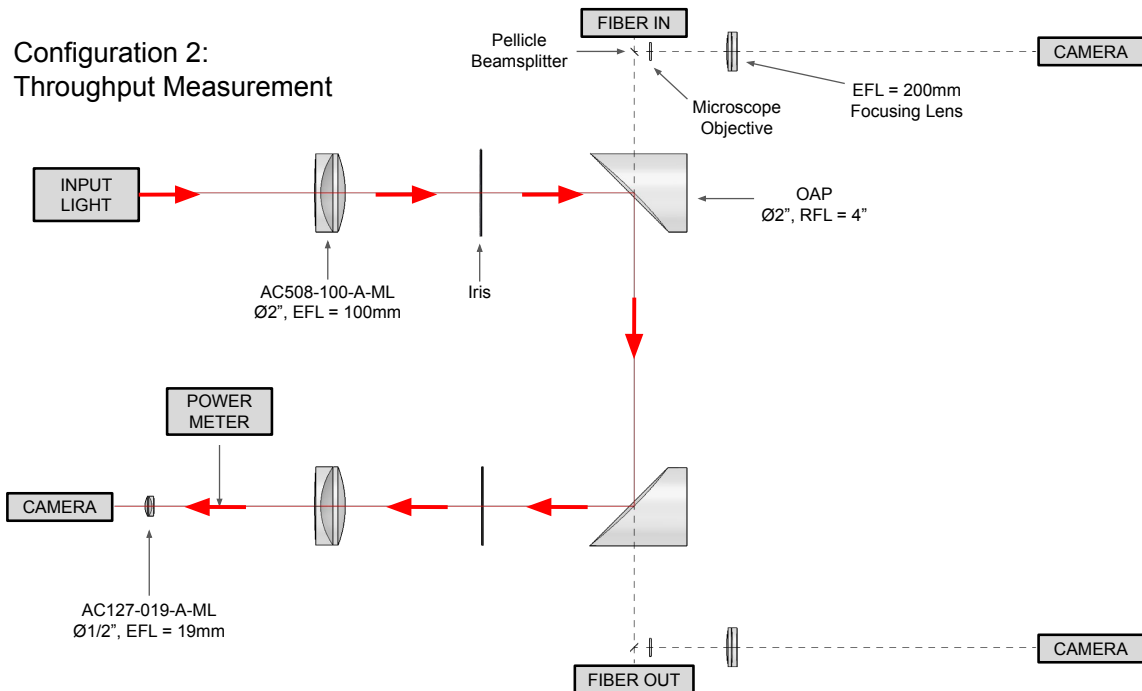


Figure 2.3: Configuration 2 of the FCS. Notice that compared to Figure 2.2, both OAPs are rotated by 180°.

Figure 2.3 shows the second configuration of the FCS. In the second configuration, the OAPs are rotated 180° to bypass the fiber. Light from the injection arm instead directly goes to the far field arm. The purpose of this configuration is to allow for the throughput of the FCS system to be accounted for when taking measurements of the output power from the fiber. The lenses and mirrors in the FCS will not have perfect transmission and reflection respectively, and so there will be some loss due to the components in the FCS. The loss due to only the fiber is the difference between the power measured in this configuration and the power measured in configuration 1.

In addition to measuring loss in the fiber, this configuration is necessary for FRD measurements. This is done by adjusting the iris diaphragms. Let the irises in the injection arm and far field arm be called iris 1 and iris 2 respectively. Suppose that we want to measure the FRD for a particular starting focal ratio N . To do this, firstly, adjust iris 1 so that the focal ratio of the input beam being injected into the fiber is N . Then, measure the power in configuration 2, in which the fiber is bypassed. After this value is recorded, switch to configuration 1, in which light is injected into the fiber, and measure the power. Due to FRD, the power of the outputted beam of the fiber will be less than the power measured in configuration 2. Then, close iris 2 until the measured power is close (e.g. 90%) to the measured power in configuration 2. Suppose to do this, we need a focal ratio of N' for iris 2. Hence, the FRD is $N' - N$.

2.2 Pre-Injection Arm

The pre-injection arm consists of all the optical components before light is injected into the test fiber. Its purpose is to inject light into the fiber from a light source. Several light sources were used with the FCS:

- Thorlabs laser diode, 635 nm, 2.5 mW (model number LPS-635-FC)
- Hamamatsu Photonics Energetiq Laser Driven Light Source (LDLS)
- Thorlabs white light mounted LED

The LDLS and white light mounted LED both were white light sources. Light from these light sources was fed to the pre-injection arm through another fiber. This source-feeding fiber was single-mode fiber for the laser diode and mounted LED, and multi-mode fiber for the LDLS. The output light of this source-feeding fiber is the input light to the pre-injection arm.

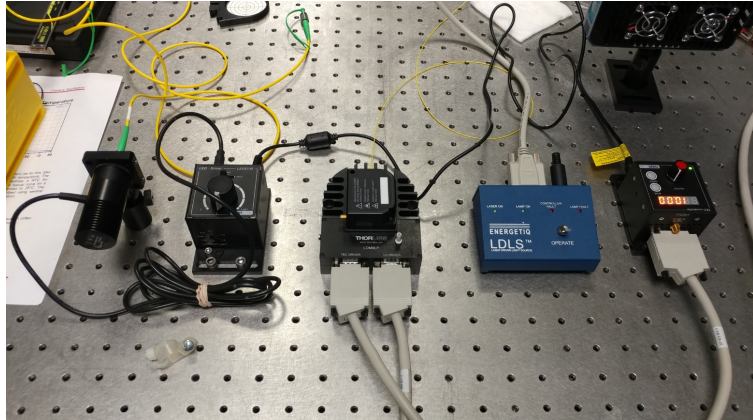


Figure 2.4: Light sources used with the FCS; from left to right: LED, LED driver, laser diode mount (Thorlabs model LDM9LP), LDLS controller, laser diode temperature controller (Thorlabs model TTC001)

The pre-injection arm uses a 60 mm cage system from Thorlabs. The output end of the source-feeding fiber is connected to the pre-injection arm by a Thorlabs SM1-threaded fiber adapter, which is held in place by an XYZ translation mount (Thorlabs model CXYZ1). The degrees of freedom offered by the XYZ translation mount allow the input light source position to be adjusted for alignment purposes. In particular, XY translation capability is needed for astigmatism correction during alignment. The cone of light outputted from the source-feeding fiber is collimated by a $\varnothing 2''$ 100 mm effective focal length (EFL) achromatic doublet lens (Thorlabs model AC508-100-A-ML).

The collimated beam of light then passes through an iris diaphragm, which is mounted on the cage system. Afterwards, the collimated beam is focused by a $\varnothing 2''$ 90° OAP with a reflected focal length (RFL) of 101.6 mm (Thorlabs model MPD249-G01) onto the input face of the test fiber. The achromatic doublet lens and OAP form a nearly one-to-one relay system due to their focal lengths; output light from the source-feeding fiber is reimaged nearly one-to-one onto the input face of the test fiber. The OAP is held by a rotation mount (Thorlabs model LCP16R2), to allow for the OAP to be rotated between the two configurations. The test fiber is held in place by a Thorlabs NanoMax multi-axis flexure stage, which allows the test fiber input position to be adjusted with precision.

Between the OAP and the test fiber is a $\varnothing 1''$ pellicle beamsplitter which directs reflected light from the fiber input face towards the injection imaging arm. Instead of other types of beamsplitters, a pellicle beamsplitter was selected because it does not cause ghosting effects and beam deviation. The pellicle beamsplitter has a reflection-transmission ratio of

45:55 (Thorlabs model BP145B1), and is oriented at an angle of 45° with respect to the path in which the focusing beam (from the OAP) is travelling. As a result of this pellicle beamsplitter, some of the incoming light which is being focused by the OAP will be reflected in the direction directly opposite of the injection imaging arm, instead of being injected into the test fiber. A beam block was added in order to absorb the reflected incoming light.

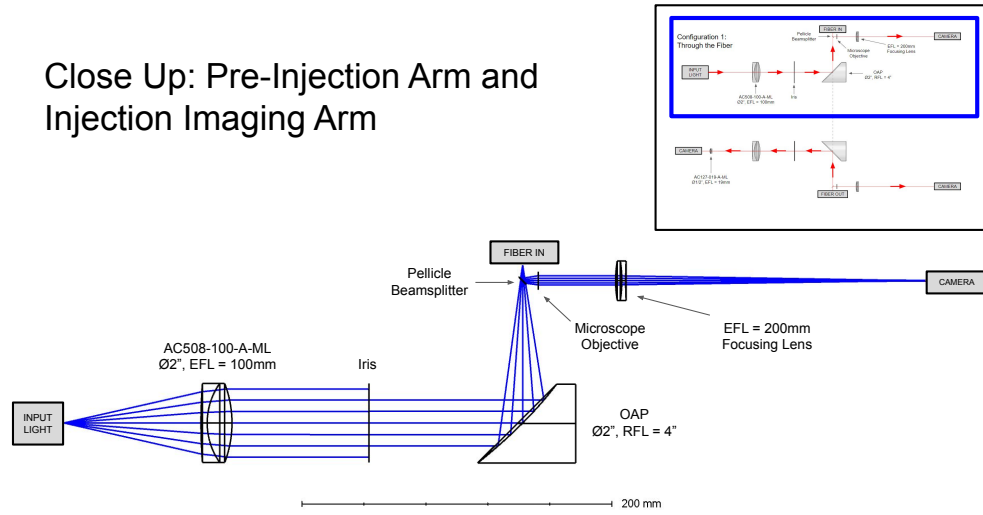


Figure 2.5: Zemax OpticStudio model of the pre-injection arm and injection imaging arm. The inset at the top right shows the location of these components in Figure 2.2.

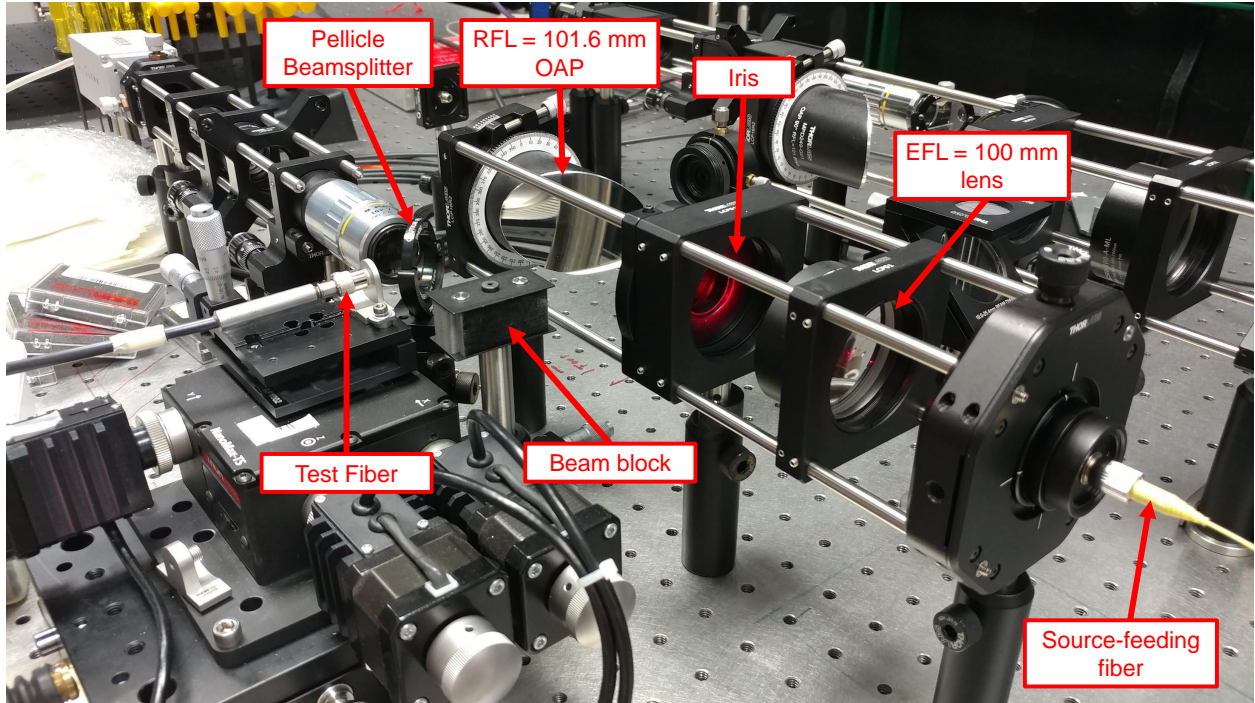


Figure 2.6: Pre-injection arm, with components labelled

2.3 Injection Imaging Arm

The injection imaging arm images the test fiber input face to ensure that the input light is correctly fed into the test fiber. It looks back at the fiber input face via the pellicle beamsplitter. The pellicle beamsplitter is mounted onto a magnetic kinematic base (Thorlabs model KB1X1) for easy removal. This apparatus is then mounted on a rotation stage (Thorlabs model RP005), which is mounted onto a XY translation stage for more movement capabilities. The reflected light from the fiber input face is reflected by the pellicle beamsplitter into the injection imaging arm. Compared to the pre-injection arm which uses a 60 mm cage system, the injection imaging arm uses a 30 mm cage system. When light enters the injection imaging arm, it is first collimated by a Mitutoyo MY10X-803 infinite conjugate microscope objective lens. The objective lens is held in place by a Thorlabs SM1A27 adapter and a Z-axis translation mount (Thorlabs model SM1ZA) with a micrometer, for alignment purposes.

The collimated beam is then focused by a $\varnothing 1''$ 200 mm EFL achromatic doublet lens (Thorlabs model AC254-200-A-ML) onto a detector. This lens is also held in place by a Z-axis translation mount. The detector is a Pixelink PL-B781U CMOS camera (2208×3000 pixels, $3.5 \mu\text{m}$ pixel pitch), and is held in place by a XY translation mount (Thorlabs model

CXY1A). Note that the objective lens and 200 EFL lens together create a microscope with a magnification of 10. On the detector, the size of the image of the fiber input face is 10 times that of the fiber input face.

The objective lens and camera cause sag in the cage system due to their mass, and hence are both supported by additional mounting brackets (Thorlabs model CP02B). In addition, note that along the cage rail, between the 200 mm EFL lens and the objective lens, is a Thorlabs LCP02 cage plate adapter which converts between the 60 mm cage system and the 30 mm cage system. This adapter is used for alignment purposes.

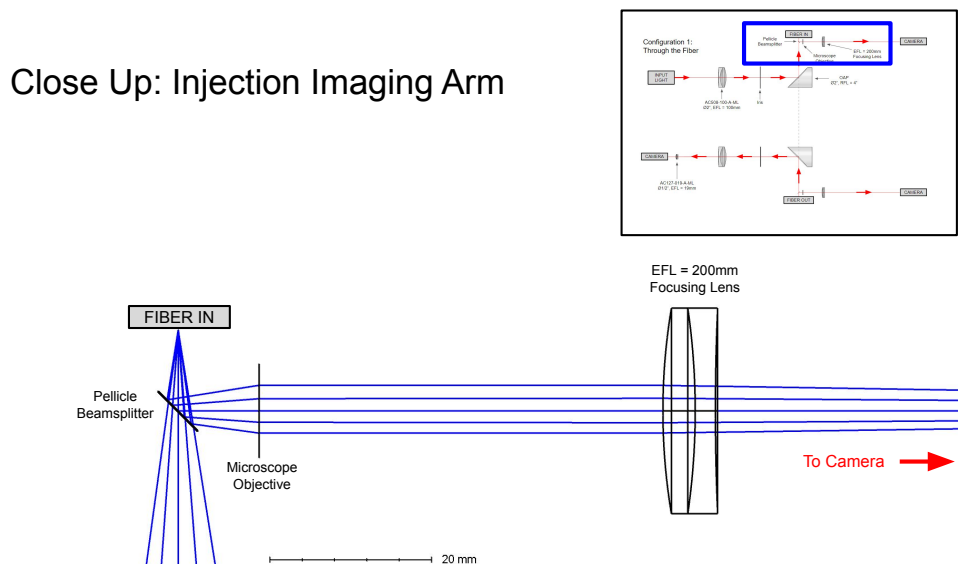


Figure 2.7: Zemax OpticStudio model of part of the injection imaging arm, from the pellicle beamsplitter to the 200 mm EFL lens. Note that the microscope objective is modelled by a paraxial lens because an actual model could not be found. The inset at the top right shows the location of these components in Figure 2.2.

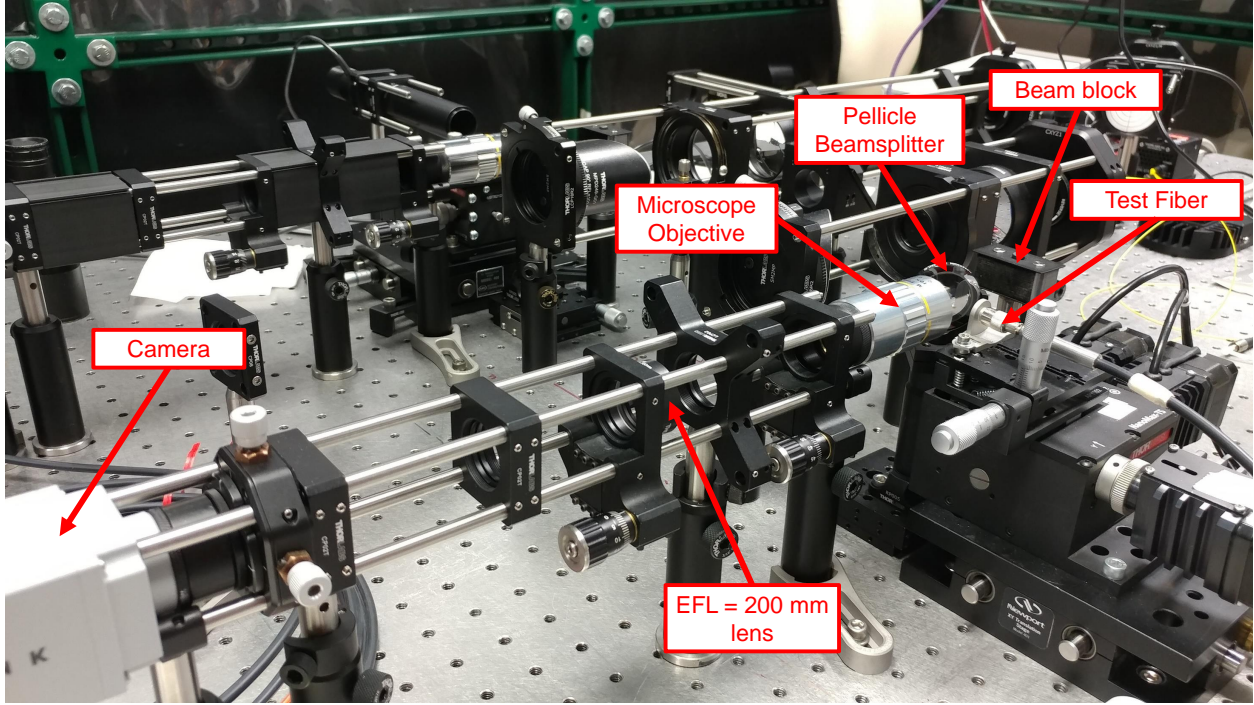


Figure 2.8: Injection imaging arm, with components labelled

2.4 Near Field Arm

The light which is injected into the test fiber travels through the fiber and exits the fiber on the other side of the FCS, which is nearly a mirror copy of the injection side. A pellicle beamsplitter (same model as the one the injection side) splits the outputted cone of the light from the test fiber into two directions. Some of the light is reflected into the near field arm, which images the near field of the test fiber (output face of the test fiber). The near field arm is nearly identical to the injection arm, except that a different camera is used. Instead, a Matrix Vision mvBlueCOUGAR-X102kG CMOS camera (1600×1104 pixels, $9 \mu\text{m}$ pixel pitch) is used. In addition, cage system covers (Thorlabs model C30L24) were used for the near field arm in order to reduce the effects of stray light.

Close Up: Near Field Arm

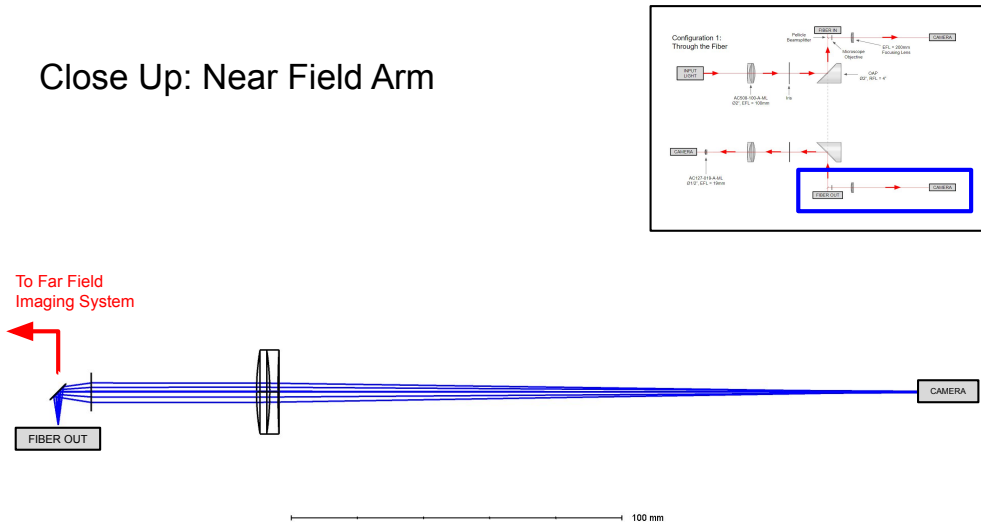


Figure 2.9: Zemax OpticStudio model of the near field arm. The inset at the top right shows the location of these components in Figure 2.2.

2.5 Far Field Arm

The rest of the light which is not reflected by the pellicle beamsplitter into the near field arm instead passes through the beamsplitter towards the far field arm. The far field arm is the same as the pre-injection arm, up until a 100 mm EFL lens. The output cone of light from the fiber is collimated by a $\varnothing 2''$ 90° OAP with 101.6 mm RFL, passes through an iris diaphragm, and then is focused by a $\varnothing 2''$ 100 mm EFL achromatic doublet lens. At the focus is a power meter, which can slide in and out of the cage system using some rails.

If the power meter is not in place, then the focused beam expands and is recollimated by a $\varnothing 0.5''$ 19 mm EFL achromatic doublet lens. Here, the cage system changes from the 60 mm cage system, down to the 30 mm cage system using a Thorlabs LCP02 cage plate adapter. The 19 mm EFL lens is held in place by Thorlabs SM1A6 adapter and a Z-axis translation mount (Thorlabs model SM1ZA) with a micrometer, for alignment purposes. After the 19 mm EFL lens, the 30 mm cage system changes back to the 60 mm cage system. The collimated beam is imaged by a Matrix Vision mvBlueCOUGAR-X102kG CMOS camera, which images the far field of the fiber. The camera is held in place by a XYZ translation mount (Thorlabs model CXYZ1). The 100 mm EFL lens and 19 mm EFL lens together create a $\sim 5\times$ beam reducer.

Close Up: Far Field Arm

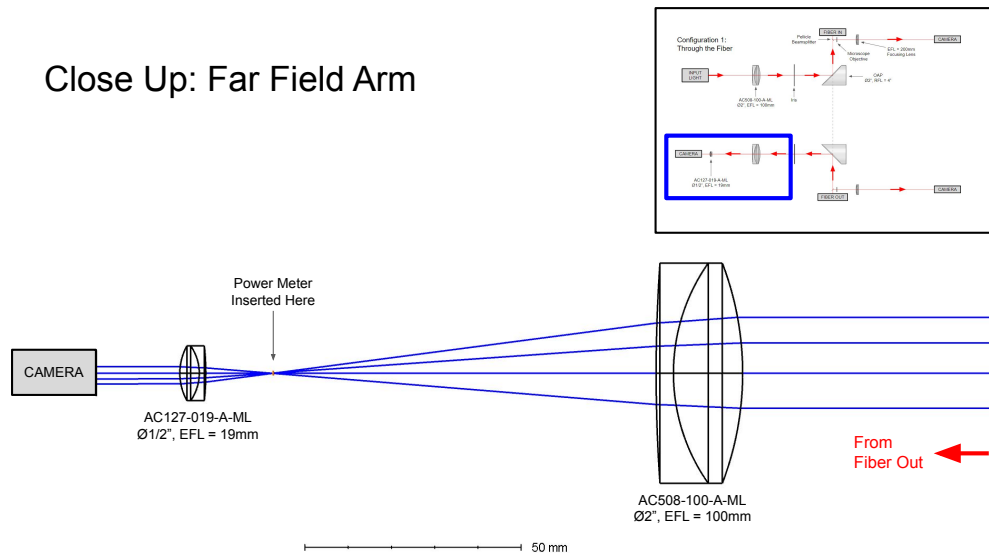


Figure 2.10: Zemax OpticStudio model of part of the far field arm, from the 100 mm EFL lens to the Matrix Vision camera. The inset at the top right shows the location of these components in Figure 2.2.

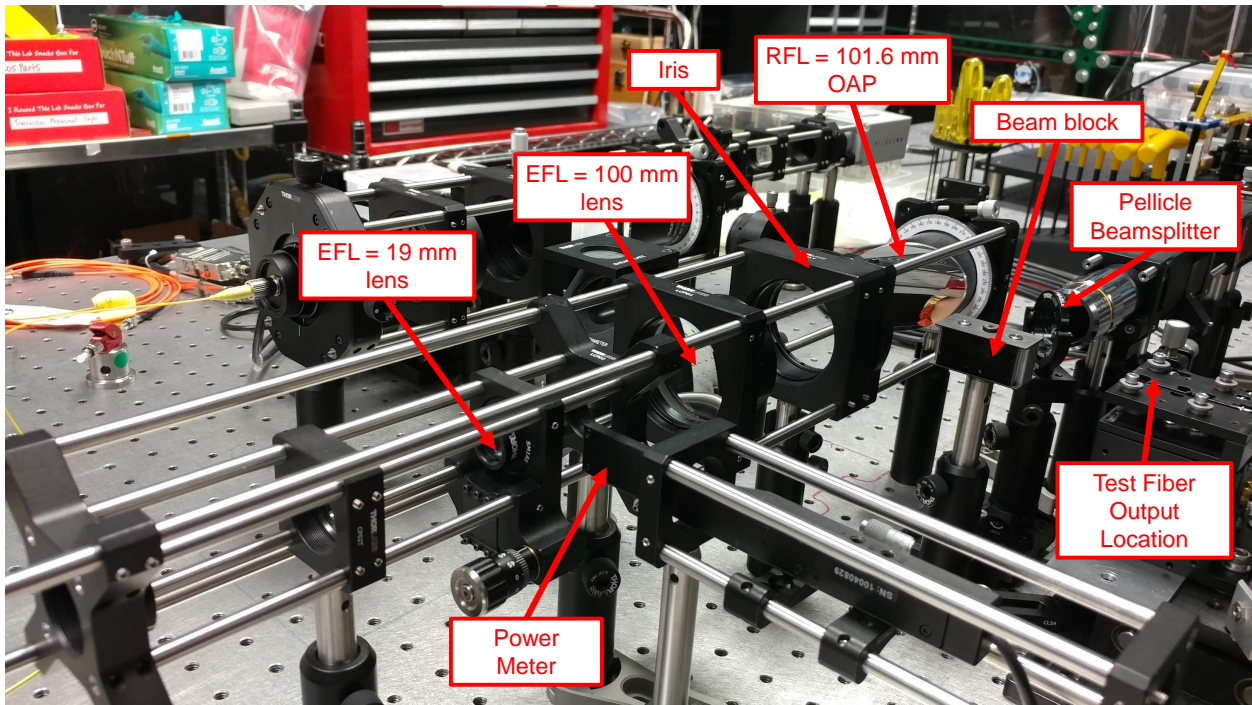


Figure 2.11: Far field arm, with components labelled

Chapter 3

Fiber Characterization Station: Assembly and Alignment

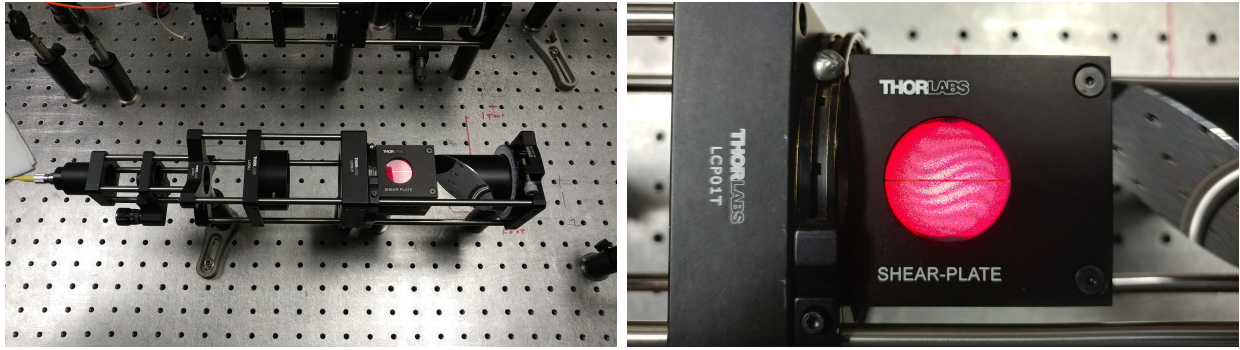
3.1 Introduction

This chapter will discuss about the assembly and alignment procedures of the FCS. Assembly and alignment is a very important phase of an instrument. In particular, alignment can often be very time consuming, and systematic approaches are required. This chapter will discuss about some tools and methods used for aligning each arm in the FCS.

3.2 Tools for Alignment

3.2.1 Shearing Interferometer

A shearing interferometer consists of a flat piece of glass oriented at 45° with respect to an incident beam. The two beams reflected by the glass (reflection from the top and bottom surfaces) interfere to produce a pattern on a diffuser plate with a marked straight line. The shearing interferometer was used to collimate optics. If a beam from a coherent source is collimated, then on the diffuser plate will be two circles of the same size overlapping, and between these two circles will be an interference pattern with fringes parallel to the marked straight line. Hence, a shearing interferometer can be used as a tool to help collimate optics. Note that due to other aberrations, the fringes may not be perfectly straight. A laser diode was used for the coherent source.



(a) Shearing interferometer in far field arm (b) Shearing interferometer diffuser plate

Figure 3.1: Using a shearing interferometer to collimate a 100 mm EFL lens in the far field arm. Note that a laser diode, which is a coherent source, is used here as the light source. The fringe pattern in Figure 3.1b shows that the lens is roughly collimated. The fringes are not perfectly straight due to other aberrations.

3.2.2 Collimated Source

Using the shearing interferometer, a collimated source setup was created, which consists of a terminated fiber adapter and a $\varnothing 2''$ 100 mm EFL achromatic doublet lens, both mounted on a 60 mm cage system. The lens collimates light coming out of a fiber connected to the terminated fiber adapter. The fiber was then connected to a source, such as the LDLS or laser diode. The lens was collimated by using the shearing interferometer to check for collimation (with a laser diode used as the source). Once collimation was achieved, all of the components were secured in place. This collimated source setup was used to align the components in the FCS which are supposed to focus a collimated beam.

3.2.3 Mini Lab Jack, Vernier Caliper, and Level

A mini lab jack and vernier caliper were together used to ensure a correct height for each of the arms in the FCS. Since each arm in the FCS is a cage system supported by Thorlabs $\varnothing 1/2''$ optical posts and post holders, the height of an entire arm can be adjusted by using a mini lab jack to lift the arm's cage. A vernier caliper was used to ensure that the height of the cage was correct, by measuring the height of the lab jack supporting the cage. A level was used to ensure that the cage was not slanted when lifted by the mini lab jack. Once a correct height was achieved, the height of the posts were locked in place. Slip-on $\varnothing 1/2''$ post collars were also used as an added measure to constrain the post heights.

3.2.4 Pair of Post-Mounted Irises

A pair of post-mounted iris diaphragms were used as a tool for alignment. The height of the irises were set so that they were the same as the intended height for the arms in the FCS. That is, the irises were both set to a height such that a beam which is parallel to the optical bench and which is passing through one of the arms would pass through both irises. A vernier caliper was used to set the heights of the irises.

3.2.5 Pairs of Cage Alignment Plates

Pairs of Thorlabs cage alignment plates (for both the 30 mm and 60 mm cage systems) were used as tools for alignment. These were used in a similar manner as the post-mounted irises.

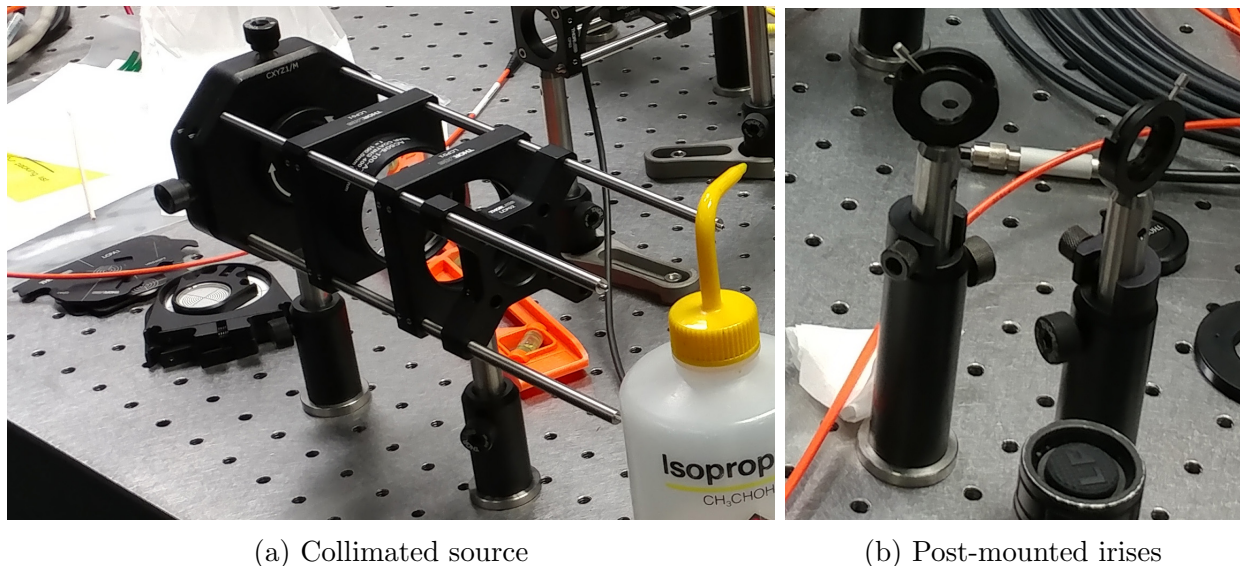


Figure 3.2: Some alignment tools: collimated source (foreground of Figure 3.2a), cage alignment plates (background of Figure 3.2a, under the orange optical fiber), and two post-mounted irises (Figure 3.2b)

3.3 Alignment Procedure for Each Arm

3.3.1 Pre-Injection Arm

To assemble and align the pre-injection arm, firstly, all of the opto-mechanical components were assembled. The pre-injection arm uses a 60 mm cage system supported by Ø1/2" optical posts. Two of the posts were held by standard Ø1/2" post holders which were screwed directly into the holes of the optical bench. Hence, the pre-injection arm runs parallel to

the long side of the optical bench. The mini lab jack was used to set the cage system to the correct height.

Once a correct height was achieved, the optical components were then placed in their intended positions in the cage. The shearing interferometer was used to align the 100 mm EFL lens so that it collimates the output from the source-feeding fiber. Next, the OAP was put in place, and was rotated until the beam reflected by the OAP (which is travelling towards the fiber injection face) was parallel to the plane of the optical bench. This was done by ensuring that the reflected beam passes through a pair of post-mounted irises.

Once the OAP was aligned, the injection position of the test fiber was adjusted so that the input face of the fiber is at the focus of the OAP. The input end of the test fiber is held by a connectorized fiber holder with a keyway that goes into a multi-axis flexure stage. In order to align the input end of the test fiber, the output side was connected to a power meter while the light source was on. Then the position of the input end of the fiber was moved using the multi-axis flexure stage until the maximum power was achieved. This is where the focus of the OAP should be.

3.3.2 Injection Imaging Arm

The injection imaging arm uses a 30 mm cage system supported by Ø1/2" optical posts. All of the posts were held by Thorlabs Ø1/2" pedestal post holders, which were secured to the table using clamping forks. To align the injection imaging arm, firstly, the height of the arm was set using the mini lab jack and vernier caliper. While setting the height of the arm, the optical components were inside the arm (but not locked in place yet) in order to account for the mass and sag of the components (in particular, the microscope objective). Next, the 200 mm EFL achromatic doublet lens was aligned using the collimated source. This lens should focus a collimated beam onto the Pixelink camera. That is, the image on the detector should be a focused Gaussian-shaped point-like spot. A custom graphical user interface (GUI) developed for the Pixelink camera was used to help with focus. This GUI will be elaborated upon later.

Next, the pellicle beamsplitter was rotated such that the beam reflected from the fiber input face would be reflected by the beamsplitter in the direction of the injection imaging arm. At this point, the injection imaging arm was moved into place. To do this, firstly the test fiber was replaced with the source-feeding fiber. That is, the source-feeding fiber was

instead plugged into the connectorized fiber holder on the multi-axis stage. The light source was then turned on. Light was now coming from where the injection occurred, and travelled towards the pellicle beamsplitter in the opposite direction. The pellicle beamsplitter then reflected the light into the injection arm. Using a pair of 30 mm cage alignment plates, the position of the injection imaging arm on the optical bench was adjusted until the beam reflected from the pellicle beamsplitter would pass through two alignment plates. This is shown in Figure 3.3. Afterwards, the lateral (XY) position of the camera was adjusted accordingly.

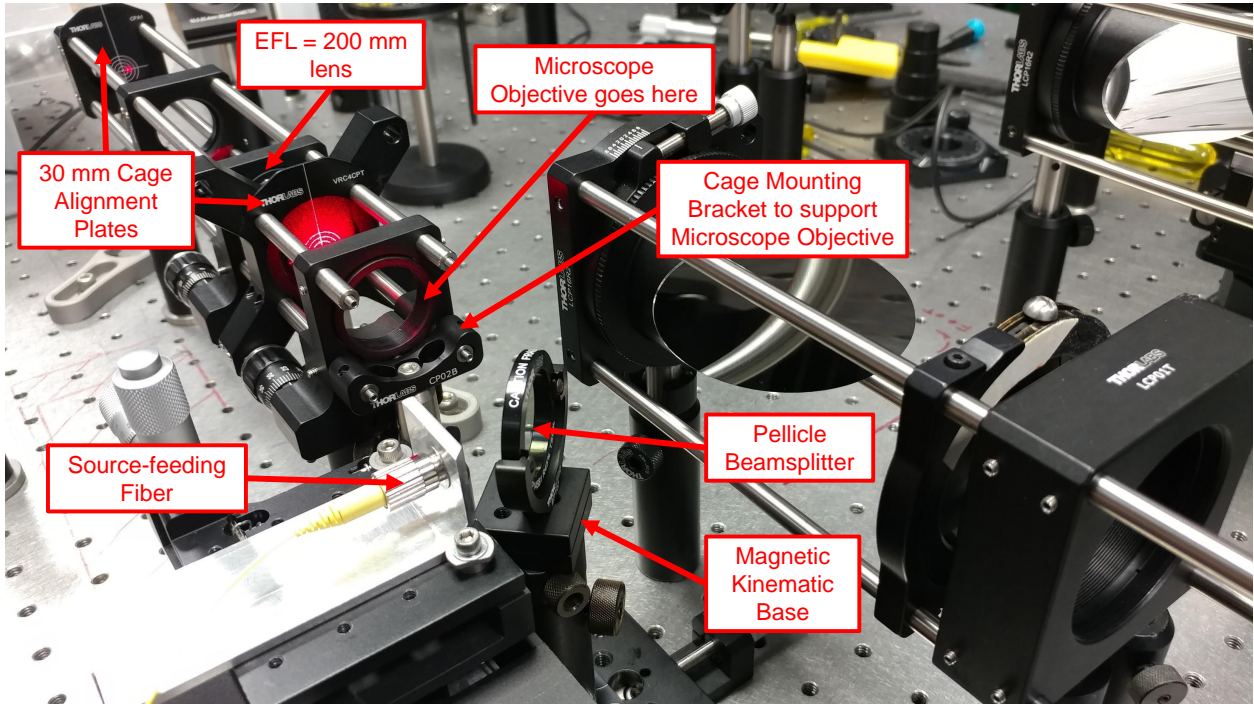


Figure 3.3: Cage alignment plates in being used when aligning the injection imaging arm. Notice that the red dot on the back alignment plate in this figure does not pass through the hole target on the alignment plate, indicating that the injection imaging arm has not been aligned yet and needs to be adjusted.

Once the correct position was achieved, the microscope objective was aligned. If the microscope objective and 200 mm EFL lens are both aligned, then the image on the detector should be a Gaussian-shaped point-like spot. This was done using the custom GUI developed for the Pixelink camera, also used to focus the 200 mm EFL lens. Code was written to acquire images from the Pixelink camera, and to fit a 2D Gaussian function to the spot in the image in real-time. The metric used as a measure of focus was the full-width at half maximum (FWHM) of the fitted 2D Gaussian function (averaged over the two FWHM values from the two axes), in units of pixels. A smaller average FWHM value implies better focus.

3.3.3 Near Field Arm

Since the near field arm is nearly identical to the injection imaging arm, the alignment procedure for the near field arm was nearly the same as that for the injection imaging arm. The mini lab jack was first used to set the height of the arm. Then the 200 mm EFL lens was aligned using the collimated source setup, ensuring that the lens focuses a collimated beam onto the detector. The arm was then moved into place, with alignment determined by the cage alignment plates. Lastly, the microscope objective was aligned. For the near field arm, a Matrix Vision camera was used instead of the Pixelink camera, and so another custom GUI specific to the Matrix Vision camera was created. The alignment of the 200 mm EFL lens and the microscope objective was done using this custom GUI.

3.3.4 Far Field Arm

Next, the far field arm was aligned. Alignment of this arm was the most challenging because of the OAP, and several approaches were attempted. Alignment was done in the direction opposite to which light is supposed to travel in the far field arm.

3.3.4.1 Initial Approaches

The 19 mm EFL lens and 100 mm EFL lens were first aligned together, and then the OAP. Using a collimated source with a laser diode, a collimated coherent beam was passed into the 19 mm EFL lens, which together with the 100 mm EFL lens form a beam expander when light is travelling towards the OAP (it becomes a beam reducer in the direction opposite to this, which is the direction in which the far field arm will be operated). The 100 mm EFL lens was then adjusted until the outputted beam was collimated, using the shearing interferometer. This is shown in Figure 3.1. Once the 19 mm EFL lens and 100 mm EFL lens were aligned, the OAP was aligned using a similar procedure as for the pre-injection arm.

However, this procedure did not work well because when the far field arm was used in the intended way (light exits out of test fiber, is collimated by OAP, then passes through a beam reducer setup towards the camera), the far field image of the fiber was incorrect. For example, the far field image of a circular fiber appeared elliptical and rotated, rather than circular. The cause of this was investigated. One observation was that after the 100 mm EFL lens, the beam appeared to be still circular in shape, but that after passing through the 19 mm EFL lens, the beam becomes more elliptical in shape. Hence, it was hypothesized that the 19 mm EFL lens might be causing astigmatism or might be magnifying unwanted features due to its high angular magnification. A model of the far field arm was constructed in

Zemax OpticStudio, and a tolerance analysis was conducted. In this Zemax mode, different optical components were also tilted and moved, and the effects of these on the far field image quality were investigated. It was found that the image quality is very sensitive to the misalignment of the OAP, especially in rotation and tilt. From the Zemax simulation, the 19 mm EFL lens did not seem to affect the beam shape significantly. It was likely that the beam itself was elliptical (caused by the OAP) before the 19 mm EFL lens, and that the angular magnification of the 19 mm EFL lens just amplified the effect. The problem was likely due to the OAP.

3.3.4.2 A More Systematic Approach

Knowing that the alignment problem was most likely due to the OAP, a more systematic approach was followed. Instead, the far field arm was aligned more similar to the pre-injection arm. Firstly, the 19 mm EFL lens was removed, and only the 100 mm EFL lens and OAP were left in the arm. Now, the far field arm was nearly identical to the pre-injection arm, and hence the same procedure as in Section 3.3.1 was used to align the 100 mm EFL lens and the OAP. Once these were aligned, the 19 mm EFL lens was added back in and aligned.

Another custom GUI was developed for the far field camera, to evaluate the image quality when a circular test fiber was used. This GUI fitted an ellipse to the far field fiber image and displayed the eccentricity of the fitted ellipse. Eccentricity was used as a metric for image quality when a circular test fiber was used. The far field image of the circular fiber should not appear elliptical, and so an eccentricity value closer to 0 is desired. After further adjustments to the OAP while using the GUI, eccentricity values of ~ 0.2 were obtained for the far field image of a circular fiber. This is satisfactory, but it was found that the beam had to be off-axis in order for the far field image to not appear elliptical. Several other attempts were made, with the order of alignment done in both directions, but the far field arm was unable to be aligned such that both the beam was on-axis and the image quality was acceptable.

3.3.4.3 Next Steps

Further investigations and simulations showed that the OAP was causing many issues when used to collimate light outputted from the test fiber. There were many aberrations which could not be resolved. The far field arm would be easier to align if the OAP was simply replaced by a flat mirror mounted on a pivoting quick-release mount and a 100 mm EFL lens. This would be a next step.

3.4 Camera Control Software and Custom Alignment GUI Tools

This section will briefly describe the software used to control the cameras and the custom GUI tools developed to aid in alignment, as touched upon in the previous sections. All software was written in Python. For the Pixelink camera, the Pixelink Python wrapper library¹ was used to control the camera. For the Matrix Vision mvBlueCOUGAR-X102kG cameras, the Harvester Python library² and the Matrix Vision mvIMPACT Python library were used to control the cameras. The Harvester library was used for the GUIs involving the mvBlueCOUGAR-X102kG cameras, but the mvIMPACT library was used when acquiring actual images for the mode scrambler experiments in the following chapter. There were various significant issues when using the mvIMPACT library with the mvBlueCOUGAR-X102kG cameras (e.g. issues in frame rate caused by Ethernet MTU), but these will not be discussed in detail in this report.

Figure 3.4 shows the custom GUI used for aligning the injection imaging arm, made using the Matplotlib Python library and the Pixelink Python wrapper. Specifically, this program was used to align the 200 mm EFL lens so that it focuses the collimated beam (collimated by the microscope objective) onto the camera. This program continuously and automatically acquires images using the Pixelink camera in the injection imaging arm, identifies a region of interest encompassing the spot in the image, and fits a Gaussian function to that spot, all in real-time. A plot of the fitted Gaussian's average FWHM is shown as a function of time. Using this, a user can determine where the 200 mm EFL lens will be in focus.

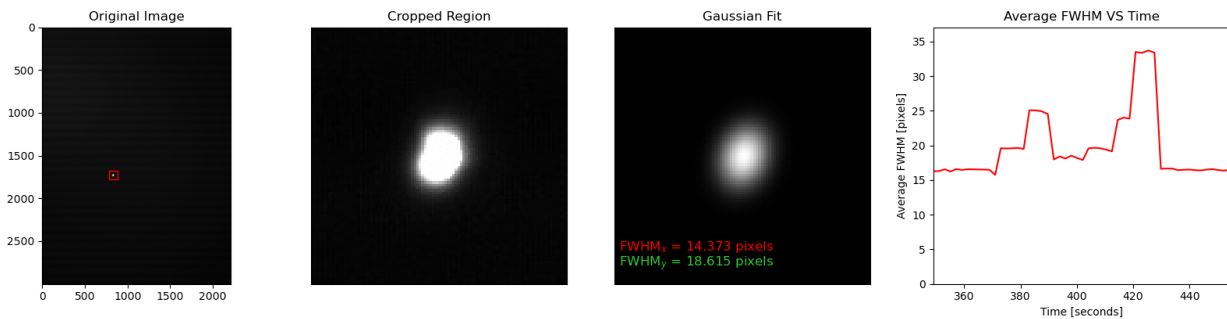


Figure 3.4: Custom GUI for injection imaging arm, made using the Matplotlib Python library and the Pixelink Python wrapper. The plots update in real-time, with the rightmost plot showing the fitted FWHM as a function of time.

¹See: <https://pypi.org/project/pixelinkWrapper/>

²See: <https://harvesters.readthedocs.io/en/latest/>

Figure 3.5 shows the custom GUI used for aligning the near field arm, made using the PyQtGraph Python library and the Harvester Python library. Specifically, this program was used to align the 200 mm EFL lens so that it focuses the collimated beam (collimated by the microscope objective) onto the camera, like in the GUI for the pre-injection imaging arm. The main difference here is that this GUI is for the mvBlueCOUGAR-X102kG camera instead of the Pixelink camera, and also has an improved and faster interface created using PyQtGraph instead of Matplotlib. The user can select a region of interest in the leftmost plot which will be used to fit a Gaussian function over. Like in the GUI for the Pixelink camera, a plot of the fitted Gaussian's average FWHM is shown as a function of time.

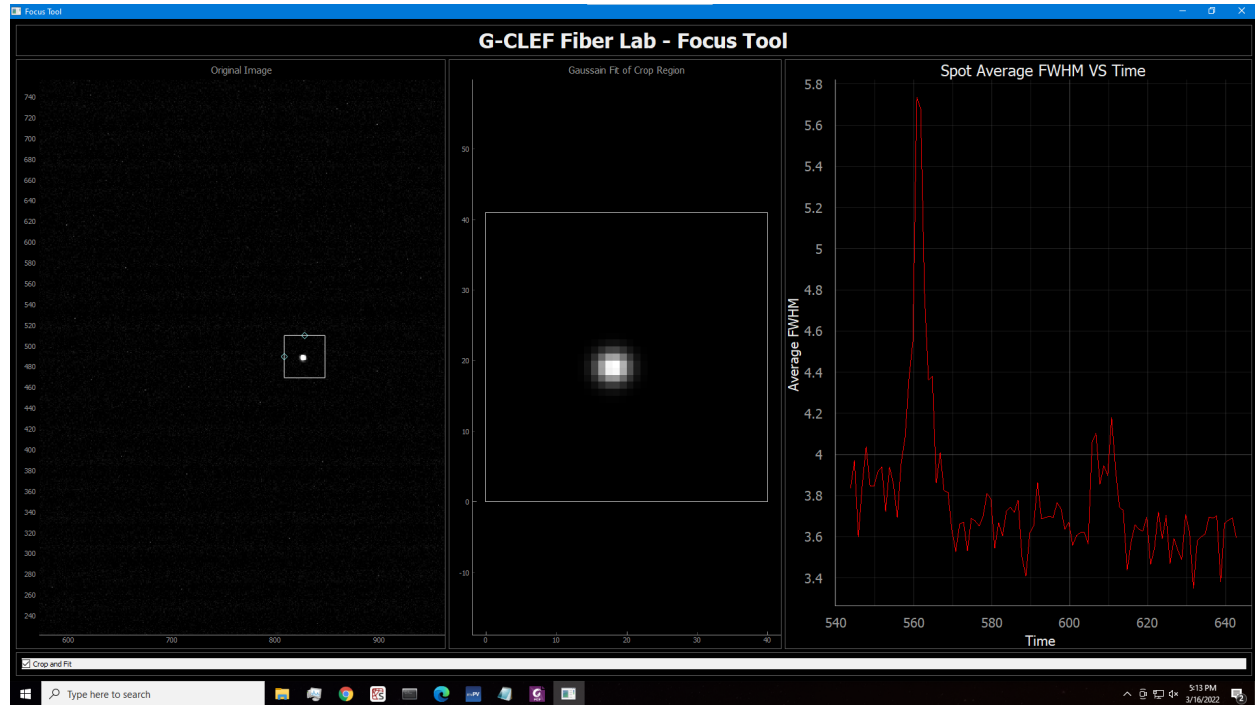


Figure 3.5: Custom GUI for near field arm, made using the PyQtGraph Python library and the Harvester Python library. The plots update in real-time. A user can select a region of interest in the leftmost plot to fit a Gaussian function, and the rightmost plot shows the fitted FWHM as a function of time.

Figure 3.6 shows the custom GUI used for aligning the far field arm, again made using the PyQtGraph Python library and the Harvester Python library. If the far field arm is aligned, then the far field of a circular test fiber should be circular shaped. Otherwise, the far field could appear elliptical. This program continuously and automatically acquires images using the mvBlueCOUGAR-X102kG camera in the far field arm, fits an ellipse to the far field image, and computes the eccentricity of this fitted ellipse, all in real-time. The eccentricity

value is displayed and also plotted as a function of time, so that a user can adjust optical components (e.g. OAP) accordingly to improve image quality.

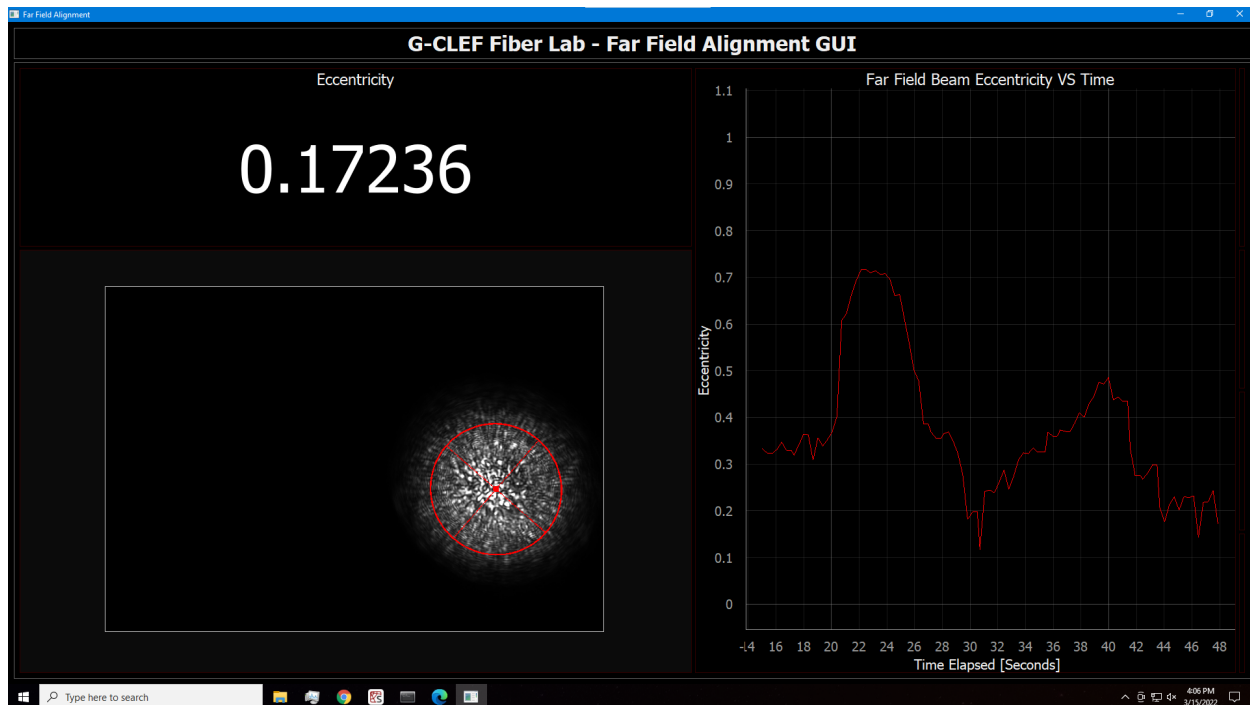


Figure 3.6: Custom GUI for far field arm, made using the PyQtGraph Python library and the Harvester Python library. An ellipse is fitted to the far field image, and the eccentricity of this fitted ellipse is plotted as a function of time in the rightmost plot. Eccentricity was used as a metric for alignment in the far field arm. Here, the eccentricity was satisfactory, but only achieved when the beam was off-axis.

Chapter 4

Mode Scrambler: Design

4.1 Introduction

This chapter will discuss about the design of the prototype fiber mode scrambler. The mode scrambler prototype consists of two stepper motors that move simultaneously at different periods and amplitudes. These two motors drive some mechanism that agitates the test fiber. Two different mechanical designs were used and tested, and these will be discussed in Section 4.2. Section 4.3 will discuss about the electrical and hardware design. Section 4.4 will discuss about the control software.

4.2 Mechanical Design

This section will discuss about the two mechanical designs for the mode scrambler prototype. Both designs use NEMA 17 bipolar stepper motors with 59 N · cm torque and a shaft diameter of shaft diameter of Ø5 mm. These motors are responsible for driving a mechanism which agitated the fiber.

4.2.1 Design 1: Simple Rotating Arm

The first mechanical design for the mode scrambler consists of a single rotating arm for each stepper motor. For each motor, a long wooden stick with periodic holes drilled into it was attached to the motor shaft using a flange. The periodic holes drilled through the stick are 1" apart, and were drilled at distances 3" to 7" away from the motor shaft, for a total of five holes. This wooden stick is the rotating arm. A test fiber passes through the holes drilled into the arm, and when the arm is rotated, the fiber is agitated. When the mode scrambler is turned on, the arm rotates from 0° to 180° and then back to 0°, and this motion

is repeated. Note that the motor changes its direction of rotation at 0° and 180° . This design was investigated because this type of motion, with a rotating arm, was not common for designs of mode scramblers in the literature.

In this design, the fiber could be passed through any one of the five holes, or all of the holes at once. The distance between the motor shaft and the fiber is an independent variable. Other independent variables include the frequency and period of the rotating arm. The effects of these independent variables on scrambling was investigated, and will be reported in the next chapter.

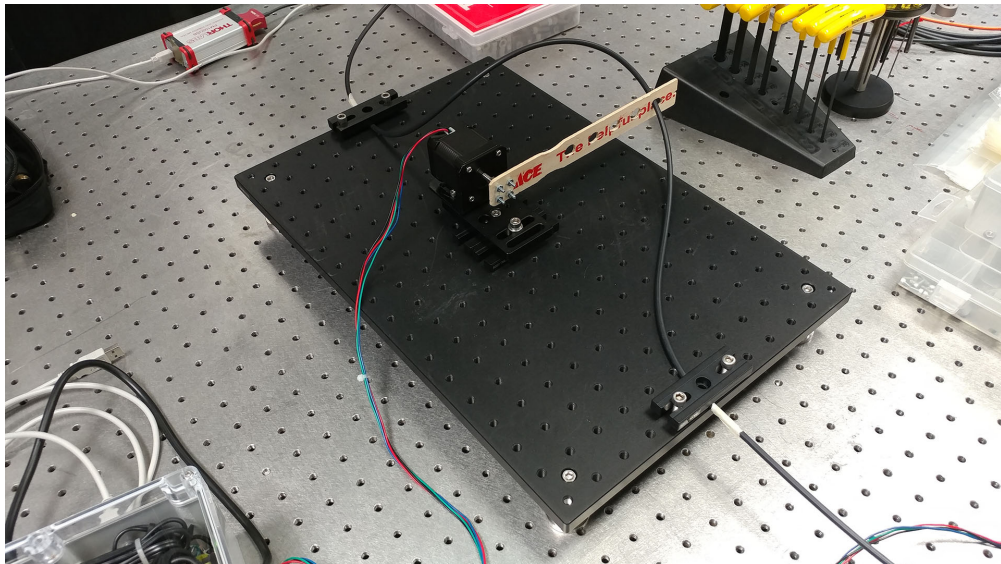


Figure 4.1: Prototype mode scrambler with a single arm design, for one motor. The test fiber is the black cable, and is clamped down to the black optical breadboard.

4.2.2 Design 2: Four-bar Linkage Crank-Rocker

The second mechanical design for the mode scrambler is a four-bar linkage crank-rocker for each stepper motor. A four-bar linkage crank-rocker can achieve a similar motion as the simple rotating arm in Section 4.2.1, but is easier to drive than the simple rotating arm. A diagram of this crank-rocker design is shown in Figure 4.2 below. In this figure, points M and Q , which have the triangle, are fixed. Bar MQ is fixed and does not move. The motor is attached to point M and rotates bar AM continuously without changing direction. The fiber is attached to bar BQ , which rotates about point Q and agitates the fiber. For a crank-rocker, $a + b < c + d$.

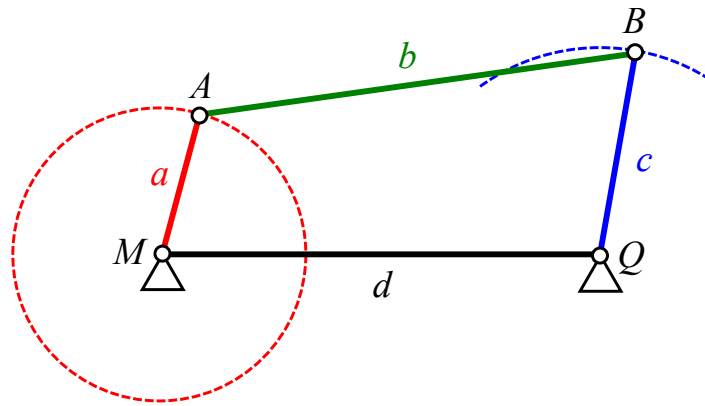


Figure 4.2: Four-bar linkage crank-rocker illustration

In this design, the lengths of the bars satisfied $b = d = 3a$ and $a = \frac{5}{7}c$. An example set of measurements is $b = d = 15$, $a = 5$, and $c = 7$. When this design was constructed, bar BQ was actually made longer, and extended beyond point B , allowing for the fiber to take on more positions along the bar. Here, the distance between the fiber (which is attached to bar BQ) and point Q is analogous to the distance between the fiber and motor shaft in Section 4.2.1, and is an independent variable. Another independent variable is the frequency at which the motor is rotating bar AM . The effect of these independent variables on scrambling was investigated, and will be reported in the next chapter.

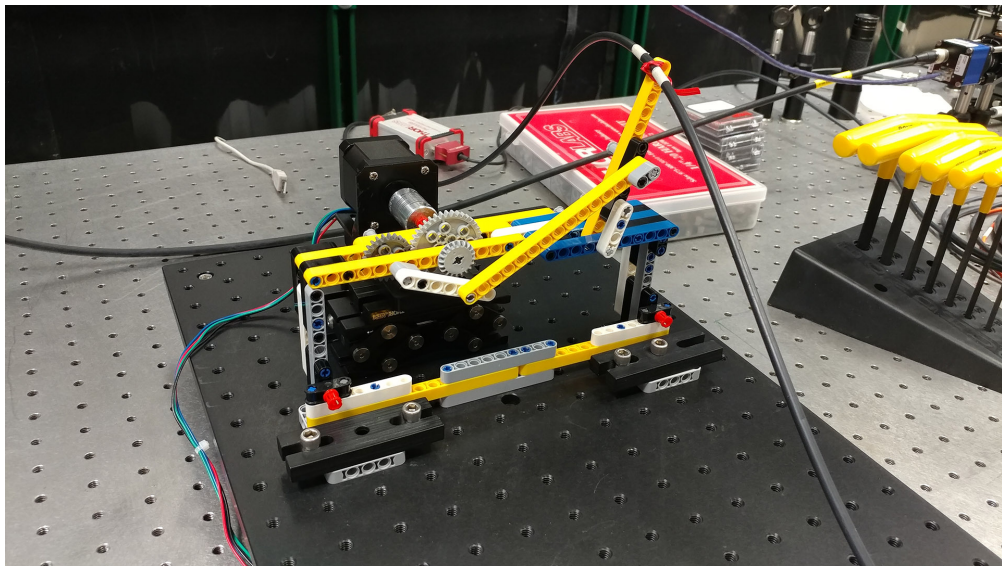


Figure 4.3: Prototype mode scrambler with a four-bar linkage crank-rocker design, for one motor. The test fiber is the black cable, and is tied down to bar BQ . Note that here, the motor shaft is not directly attached to point M , but instead a gear system is used with a 40:24 gear ratio.

4.3 Electrical and Hardware Design

A schematic of the electrical and hardware design for the mode scrambler prototype is shown in Figure 4.4. Each stepper motor (M1 and M2 in schematic) is controlled by an Arduino UNO R3 (XA1 in schematic), using A4988 stepper motor drivers (A1 and A2 in schematic).

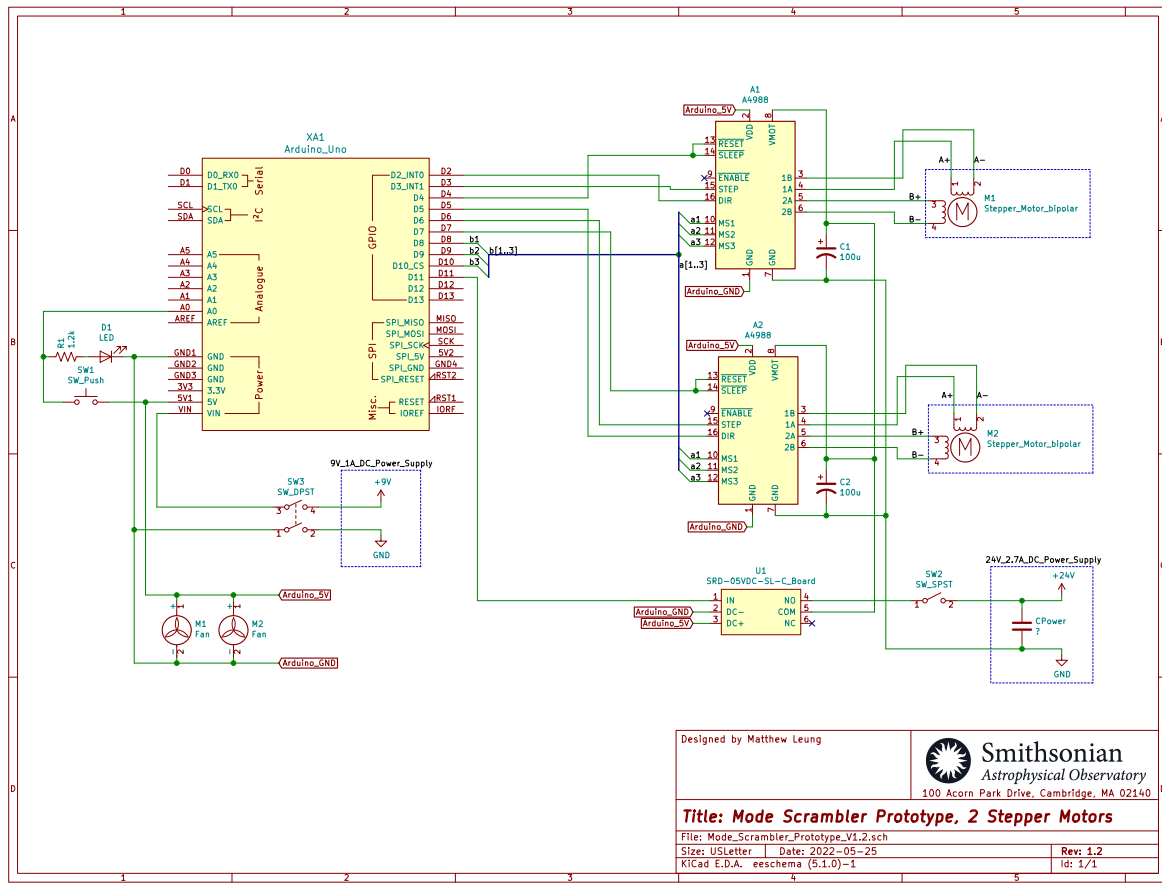


Figure 4.4: Schematic of the electrical and hardware design for the mode scrambler prototype

4.3.1 Stepper Motor Drivers

The A4988 stepper motor drivers are rated to provide 1 A to each motor, or 2 A with cooling. In order to allow for more current draw without burning the A4988 driver, a heat sink was added to each of the A4988 drivers as well as two fans for cooling. The fans have an airflow of 6 cubic feet per minute and are powered by the Arduino 5 V line. The potentiometer screw on each A4988 was adjusted to set the current limit to a more conservative value of

~1.5 A. The A4988 drivers are powered by the Arduino 5 V line, and its pins (RESET, SLEEP, STEP, DIR, MS1, MS2, MS3) are connected to the Arduino digital pins. 100 μ F electrolytic capacitors (C1 and C2 in schematic) were added across the VMOT and GND terminals of each of the A4988 drivers to reduce voltage spikes, preventing damage to the A4988 drivers.

4.3.2 Power

The motors are powered by a 24 V 2.7 A DC power supply, shown at the bottom right of the schematic. The Arduino is powered by a 9 V 1 A DC power supply. Both of these power supplies are connected to a 120 V AC line, which is connected to a standard electrical outlet. There are several safety features incorporated in this design. In order for the motors to be powered, the Arduino must be first on. Switch SW3 in the schematic connects the Arduino to the 9 V 1 A DC power supply. Once the Arduino is on, there are two steps in order for the motors to be powered. The switch SW2 must be closed. Then if a user presses button SW1, relay U1 (which is normally open) will be closed, and the motors will be connected to the 24 V 2.7 A DC power supply. If power is lost to the Arduino, then power will automatically be cut to the motors due to relay U1.

4.3.3 Electronics Box

All of the electrical and hardware components were placed inside an electronics box. Holes were drilled into the sides of the box to accommodate the two fans, switches, and other components. An IEC connector with a switch was added to the box so that the mode scrambler could be easily powered by one plug to a wall socket. A panel-mount USB adapter was added to the side of box so that the Arduino could be accessed without opening the box.

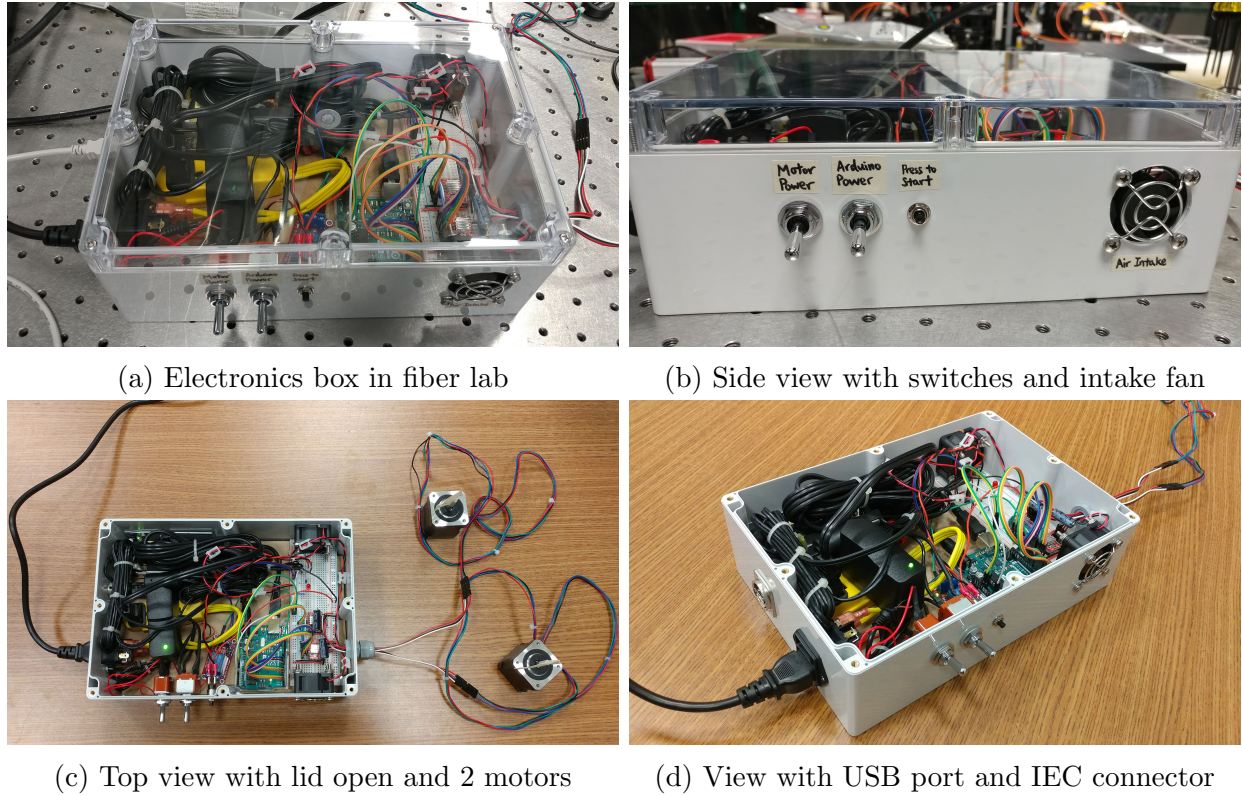


Figure 4.5: Electronics box

4.4 Control Software

4.4.1 Overview

The stepper motors were controlled by the Arduino, using the AccelStepper library. This library was used because it could control multiple motors simultaneously at different speeds. A C++ wrapper class was created to allow for easy modification of the motor frequency, target position, microstep mode, and other desired variables. The two different mechanical designs described in Section 4.2 required different programmed angular velocity profiles for the motor, and these will be described below.

4.4.2 Angular Velocity for Specific Designs

4.4.2.1 Design 1: Simple Rotating Arm

For the simple rotating arm, each motor rotates from 0° to 180° , then back to 0° , and then repeats this motion. Several angular velocity profiles for the motor were tested, and these are shown in Figure 4.6. The most simplest case is a profile in which the angular

velocity is constant, goes to zero, then switches sign, goes to zero, then repeats (Figure 4.6a). In an attempt to avoid slipping due to the motor suddenly stopping, other angular velocity profiles involving accelerations were also tested, such as triangular (Figure 4.6b) and trapezoidal (Figure 4.6c) angular velocity profiles.

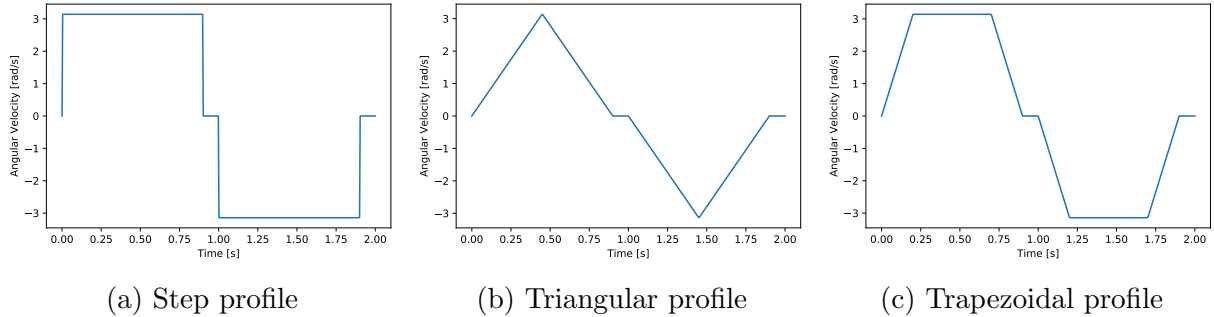


Figure 4.6: Example angular velocity profiles

4.4.2.2 Design 2: Four-bar Linkage Crank-Rocker

For the four-bar linkage crank-rocker, each motor just continuously rotates at a constant angular velocity. There is no change, unlike for the single rotating arm. This velocity profile was much simpler.

Chapter 5

Mode Scrambler: Testing and Analysis

5.1 Introduction

This chapter will discuss about the testing of the mode scrambler and the analysis of the results. The focus here will be on images taken of the fiber near field, which are images of the fiber output face or exit surface. Scrambling will be measured using these images. Various experiments were conducted, in which a particular parameter was varied (e.g. motor frequency) and fiber near field images were taken. A greater focus was placed on octagonal and rectangular fibers, which are more likely to be used to feed G-CLEF.

5.2 Performance the Two Mechanical Designs

When the simple rotating arm design (Section 4.2.1) was tested, the stepper motor frequently slipped at the moment it was changing direction. This was particularly the case when motor was being driven at higher frequencies, but sometimes occurred for lower frequencies as well. Slipping also occurred when a more stiff fiber was used, indicating that this was due to the motor not having enough torque. Instead of using a constant angular velocity profile (Figure 4.6a), other angular velocity profiles were also used, as discussed in Section 4.4.2. However, the motor still slipped. A stepper motor's method of operation is not really intended for this kind of motion. Hence, the four-bar linkage crank-rocker design (Section 4.2.2) was used instead. In this design, the stepper motor did not slip, and the type of motion for fiber agitation was similar to the simple rotating arm.

5.3 Analysis Code

This section will discuss about the analysis code used to analyze images taken of the near field fiber. All of the analysis code was written in Python. The near field arm uses a Matrix Vision CMOS camera which takes images in 12 bit. During each experiment, in addition to taking images of the near field (science frames), dark frames, bias frames, and flat field frames were also taken. After obtaining a corrected image (dark and bias subtracted, and flat field corrected), the main goal is to identify the boundary of the fiber face in the corrected image. Then some metric for scrambling can be computed from the pixels inside the fiber face boundary.

5.3.1 Dark, Bias, and Flat Field Correction

While conducting each experiment, dark frames, bias frames, and flat field frames were taken in addition to the science frames. The dark frames had the same exposure time as the science frames and were taken when a lens cap was covering the camera. The bias frames were taken with the shortest exposure time possible for the camera, and were taken when a lens cap was covering the camera. The flat field frames were taken with an evenly-illuminated diffuse light source illuminated into the near field arm. The diffuse light source consisted of two Thorlabs ground glass diffusers (Thorlabs model DG10-120) in front of a 60 mm EFL lens which collimated a white light LED.

Let SCI, DARK, BIAS, and FLAT be the science, dark, bias, and flat frames respectively. Let t_{SCI} , t_{DARK} , and t_{FLAT} be the exposure times of the science, dark, and flat frames respectively. Then the corrected image can be found by¹:

$$\text{CORRECTED} = \overline{\text{FLATCORRECTED}}_{\text{avg}} \times \left[\frac{(\text{SCI} - \text{BIAS}) - \frac{t_{\text{SCI}}}{t_{\text{DARK}}}(\text{DARK} - \text{BIAS})}{(\text{FLAT} - \text{BIAS}) - \frac{t_{\text{FLAT}}}{t_{\text{DARK}}}(\text{DARK} - \text{BIAS})} \right] \quad (5.1)$$

where:

$$\overline{\text{FLATCORRECTED}}_{\text{avg}} = \overline{\left[(\text{FLAT} - \text{BIAS}) - \frac{t_{\text{FLAT}}}{t_{\text{DARK}}}(\text{DARK} - \text{BIAS}) \right]} \quad (5.2)$$

is the average value of the flat frame (the overline denotes an average), corrected for bias and dark effects.

¹See: <http://www.bu.edu/astronomy/wp-assets/script-files/buas/oldsite/astrophotography/flat.htm>

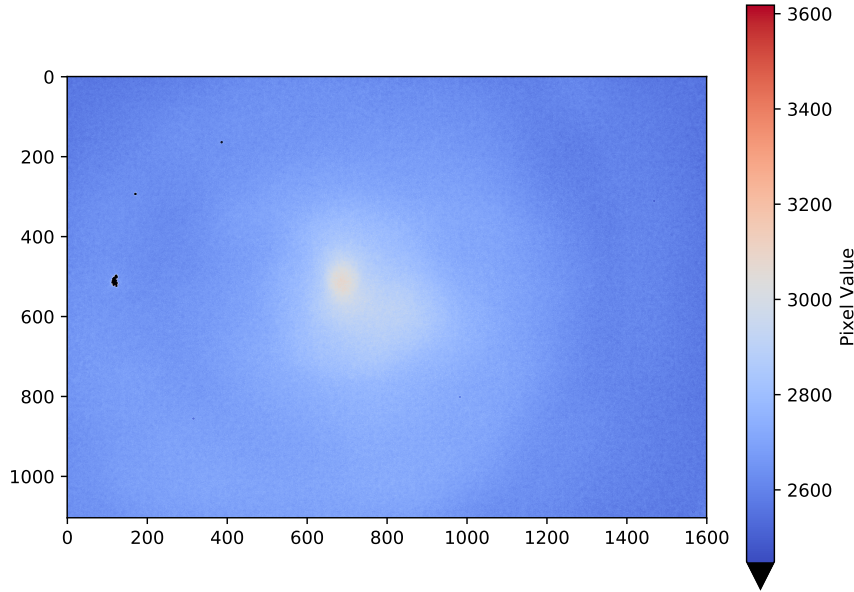


Figure 5.1: An example of a flat field image taken for the near field arm. The variation in pixel values is largely due to the pellicle beamsplitter.

5.3.2 Fiber Face Boundary Identification

After the corrections in Section 5.3.1, the next step is to identify the pixels in the corrected image which belong to the fiber face. After these pixels are identified, metrics can be computed for scrambling. The problem is as follows: given an image of a face of a fiber (near field in this case), we seek to identify the boundary of the fiber.

5.3.2.1 Ineffective Approaches

To do this, many different approaches were attempted. Initial approaches involved taking spatial derivatives of the image, using Sobel filters or Laplacian filters, in order to make the fiber boundary (edge) feature more apparent. A Canny edge detector was then applied to the filtered image (with the spatial derivative filters applied) in order to identify the boundary of the fiber face. Afterwards, the result of the Canny edge detector (which gives points representing edges) were converted into contours (lines joining the points). The longest contour was anticipated to represent the boundary of the fiber face, and an attempt was made to use Douglas-Peucker algorithm to further approximate the longest contour to reduce jaggedness in the boundary shape. However, the result of the Canny edge detector suffered from broken edges, which is a limitation commonly mentioned in the literature ([Akinlar & Chome 2016](#); [Dhillon & Chouhan 2022](#)). The resulting contours do not represent the fiber

boundary well. Thresholding was also attempted on the Laplacian-filtered or Sobel-filtered image before applying the Canny edge detector, but the results were not too generalizable.

5.3.2.2 Effective Approach: Overview

Instead of using more edge detection methods, another approach was attempted. It is important to note that the face of an optical fiber is a certain shape (e.g. circle, square, rectangle, octagon). The boundary of an optical fiber is not just some arbitrary edge. This is important information which points to computational geometry approaches instead for solving the problem of identifying the fiber face boundary. It was realized that the boundary of an optical fiber which has a convex shape (e.g. square and octagon) can be represented by a convex hull. However, some fibers may have more complicated shapes which are concave instead (e.g. a rectangular fiber which was tested in this project). The boundary of such a fiber would need to be represented by a “concave hull”. The idea of a convex hull can be generalized to something called an alpha shape ([Edelsbrunner & Mücke 1994](#)). A set of finite points can be obtained representing the entire fiber face, and the outer boundary of the alpha shape of this set of points would be the boundary of the fiber face. This approach turned out to be very effective, and is summarized by the following steps:

1. Apply Canny edge detector to an 8 bit version of the corrected image, and obtain a binary image which represents the Canny edges.
2. Take the nonzero points from the binary image, and find the alpha shape of these points.
3. Find the outer boundary of the alpha shape.
4. If desired, offset the alpha shape.

5.3.2.3 Effective Approach: Detailed Explanation

In the approach involving alpha shapes, the following was done. Firstly, the 12 bit image was converted into an 8 bit image. Canny edge detector was applied to the 8 bit image using the OpenCV implementation, and a binary image was obtained which represents the Canny edges. Let S be the set of points representing the position of the nonzero pixels in the binary image. The next step is to find the alpha shape of S , and there are several steps involved, following Edelsbrunner’s algorithm ([Edelsbrunner & Mücke 1994](#); [Fischer 2000](#)). The alpha shape is parameterized by a parameter α . If $\alpha = \infty$, then the alpha shape is the convex hull of S , and if $\alpha = 0$, then the alpha shape is just individual points ([Gardiner et al.](#)

2018). This is how an alpha shape can be thought of as a generalized version of the convex hull. If α is not a big number, then the alpha shape can be thought of as a “concave hull”.

To find the alpha shape of S given some α , firstly the Delaunay triangulation of S , called $\text{DT}(S)$, was found. This was done using SciPy. Next, the alpha complex $\mathcal{C}_\alpha(S)$ was found. $\mathcal{C}_\alpha(S)$ is a subcomplex of $\text{DT}(S)$ and consists of all simplices in $\text{DT}(S)$ such that the radius of the circumcircle of the simplex is less than α (Fischer 2000). Finally, the boundary of $\mathcal{C}_\alpha(S)$ is the boundary of the alpha shape. This boundary is made up of a set of lines represented by the lines’ endpoints. However, note that there can be both an inner boundary and an outer boundary. The outer boundary is desired, and it is assumed that the outer boundary is the boundary which has more points. Figures 5.2, 5.3, and 5.4 show this procedure applied to a near field images of an octagonal, square, and rectangular fiber respectively. $\alpha = 100$ was used for these examples. In particular, notice that the rectangular fiber does not have a convex boundary, which is why this procedure was needed.

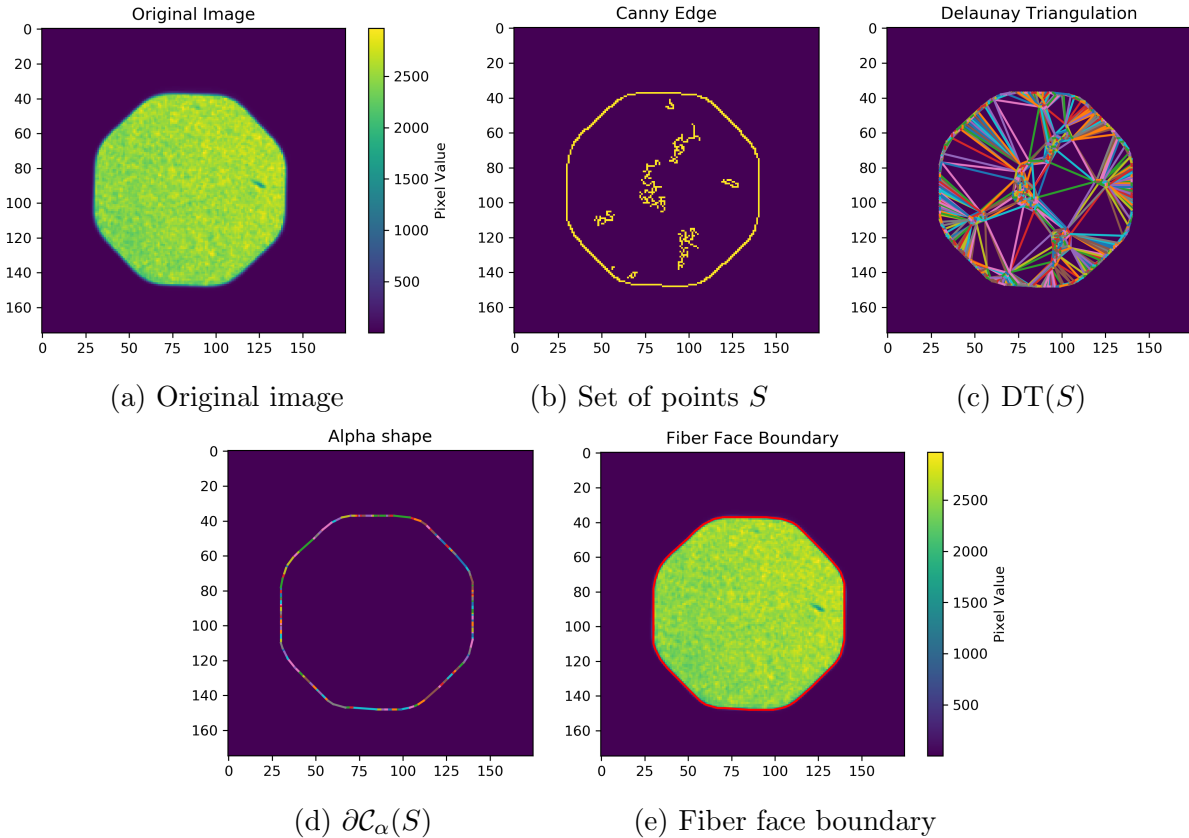


Figure 5.2: Finding the fiber face boundary in a near field image of a $100 \mu\text{m}$ octagonal fiber (Figure 5.2a, taken when the mode scrambler was on, but with only little agitation), using the procedure described in this section. Figure 5.2e shows the boundary in red.

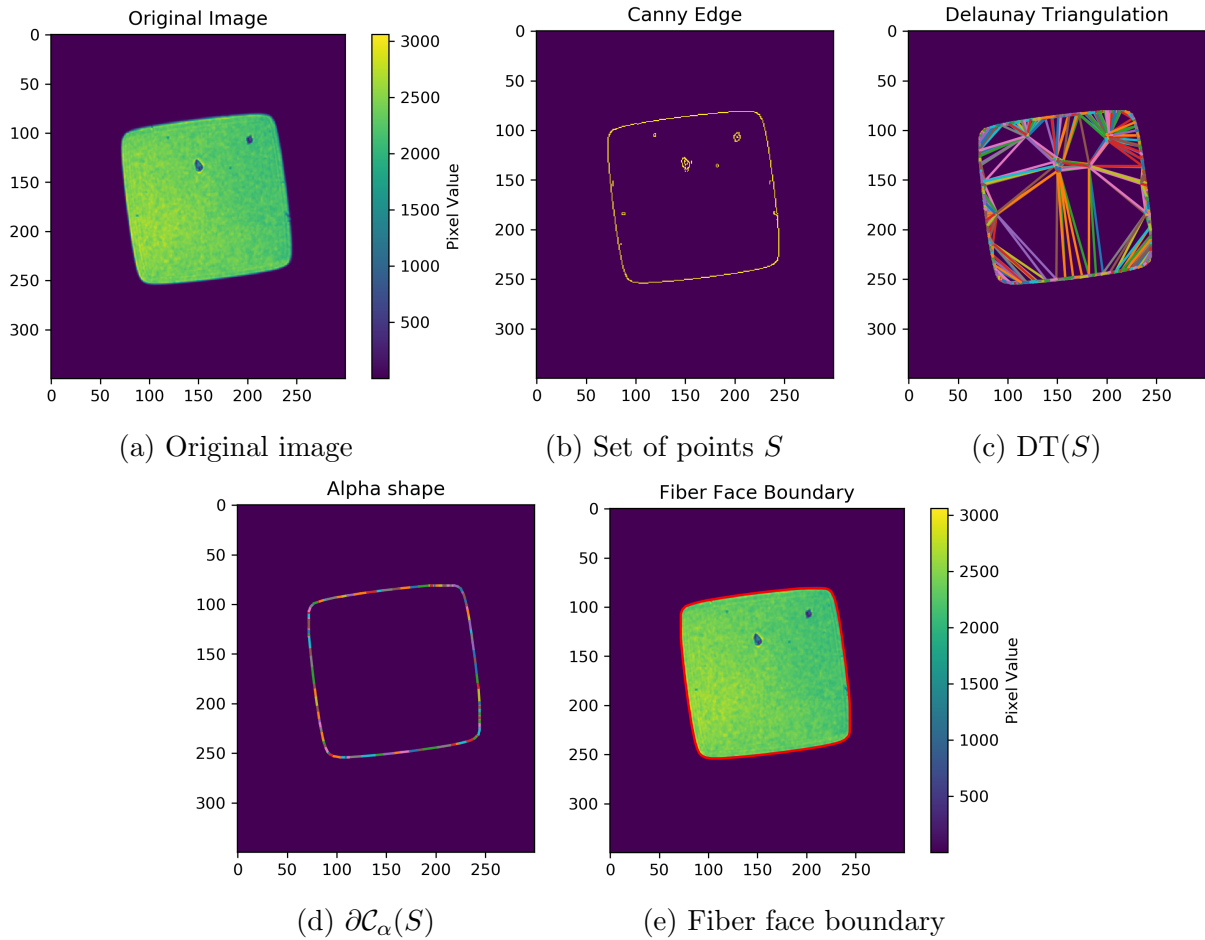


Figure 5.3: Finding the fiber face boundary in a near field image of a 150 μm square fiber (Figure 5.3a, taken when the mode scrambler was on), using the procedure described in this section. Figure 5.3e shows the boundary in red.

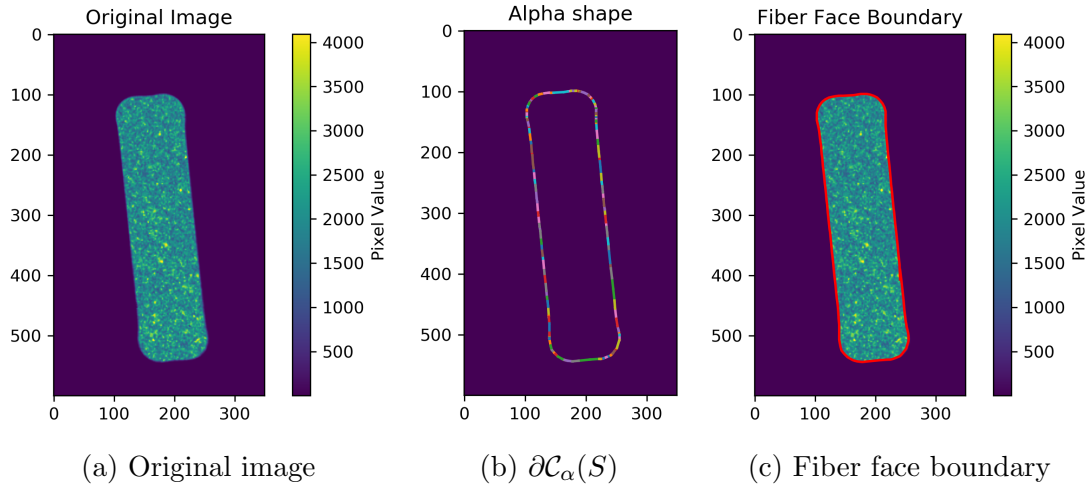


Figure 5.4: Finding the fiber face boundary in a near field image of a 400 μm by 100 μm rectangular fiber (Figure 5.4a, taken when the mode scrambler was off), using the procedure described in this section. Figure 5.4c shows the boundary in red.

Finally, the alpha shape was offset inwards by a certain number of pixels in order to account for the actual physical boundary of the fiber between the cladding and core. This was done using the Python `pyclipper` library, which is a wrapper of the C++ Clipper library². The boundary of this offset shape was taken as the boundary of the fiber face. An example of this is shown in Figure 5.5, for a rectangular fiber. With the fiber face boundary identified, metrics for scrambling can be computed from the pixels inside the boundary.

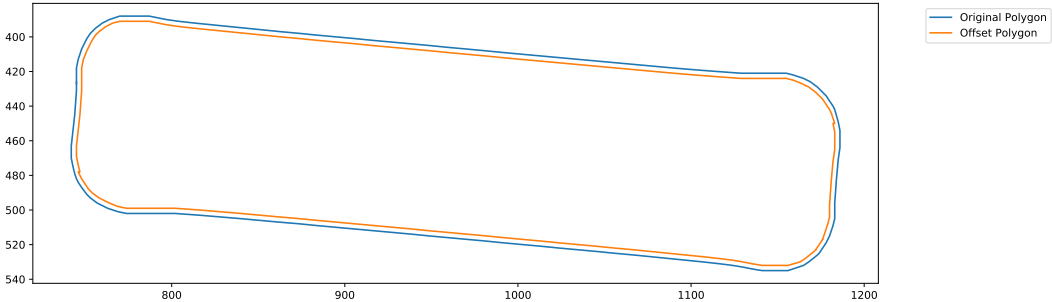


Figure 5.5: An example of a boundary being offset by 3 pixels, for a rectangular fiber. The original boundary is shown in blue, and the offset boundary is shown in orange.

²See: <http://www.angusj.com/clipper2/Docs/Overview.htm>

5.3.3 Metric for Mode Scrambling

The metric used to describe the amount of scrambling was the “signal-to-noise ratio” (SNR), which I defined as:

$$\text{SNR} \equiv \frac{\mu}{\sigma} \quad (5.3)$$

where μ and σ are:

$$\mu = \frac{1}{N} \sum_{i=1}^N x_i \quad (5.4)$$

$$\sigma = \sqrt{\frac{1}{N} \sum_{i=1}^N (x_i - \mu)^2} \quad (5.5)$$

where N is the total number of pixels inside the fiber face boundary and each x_i is the value of one pixel (corrected value). μ is the mean pixel value for the pixels inside the fiber face boundary, and σ is the standard deviation of the pixels inside the fiber face boundary. This definition was inspired by a metric used in Petersburg et al. (2018) for mode scrambling. In Petersburg et al. (2018), a quantity called the “signal-to-noise ratio” was also defined as a metric for mode scrambling, but was slightly different from the definition here in that the median is used instead of the mean and the image was firstly median filtered. The uncertainty in μ , σ , and SNR are $\delta\mu$, $\delta\sigma$, and δSNR respectively, given as:

$$\delta\mu = \frac{1}{N} \sqrt{\sum_{i=1}^N (\delta x_i)^2} \quad (5.6)$$

$$\delta\sigma = \sqrt{\sum_{i=1}^N \left[\left(\frac{x_i - \mu}{\sigma N} \right)^2 (\delta x_i)^2 \right]} \quad (5.7)$$

$$\delta\text{SNR} = (\text{SNR}) \sqrt{\left(\frac{\delta\mu}{\mu} \right)^2 + \left(\frac{\delta\sigma}{\sigma} \right)^2} \quad (5.8)$$

5.4 Results

This section will discuss about the results of some scrambling experiments conducted using both designs of the mode scrambler prototype described in Section 4.2. The effects of different parameters (e.g. motor frequency) on scrambling will be discussed. Images of the near field of a test fiber were taken using the near field arm of the FCS. In all of the following plots, the SNR when the mode scrambler was on and the SNR when the mode

scrambler was off will be displayed. When the mode scrambler is turned off, there should be no relationship between the SNR and a certain parameter.

5.4.1 Example Images

Figures 5.6 and 5.7 show images of the near field of an octagonal and rectangular fiber respectively, when the mode scrambler was off and on. Clearly, the modal noise is reduced when the mode scrambler is turned on.

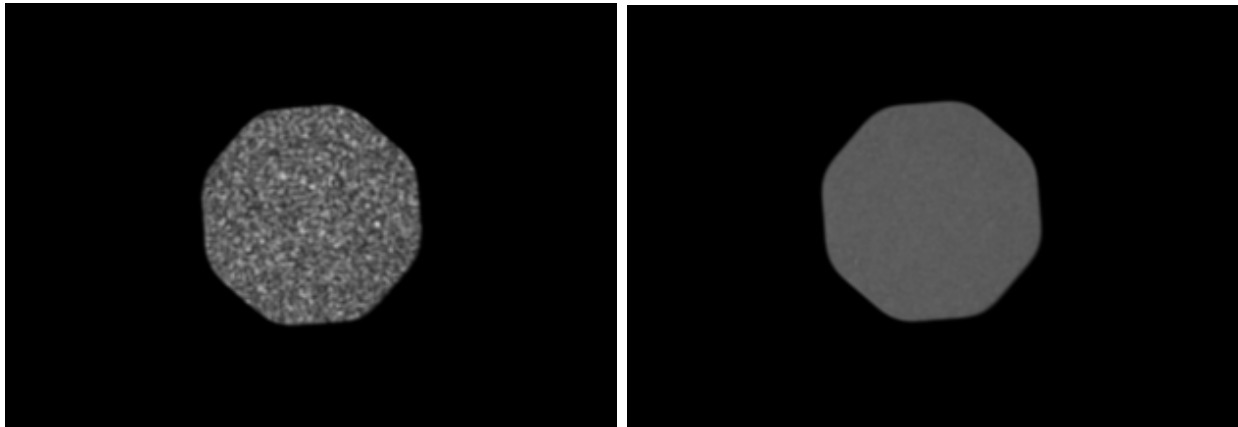


Figure 5.6: Near field images of a $100 \mu\text{m}$ octagonal test fiber, with the mode scrambler was off (Figure 5.6a) and on (Figure 5.6b). Both images are a stack of 100 frames, with each individual frame having an exposure time of $60 \mu\text{s}$. Both images were acquired when the four-bar linkage-crank rocker was used, and bar *MA* was driven at 5 Hz.

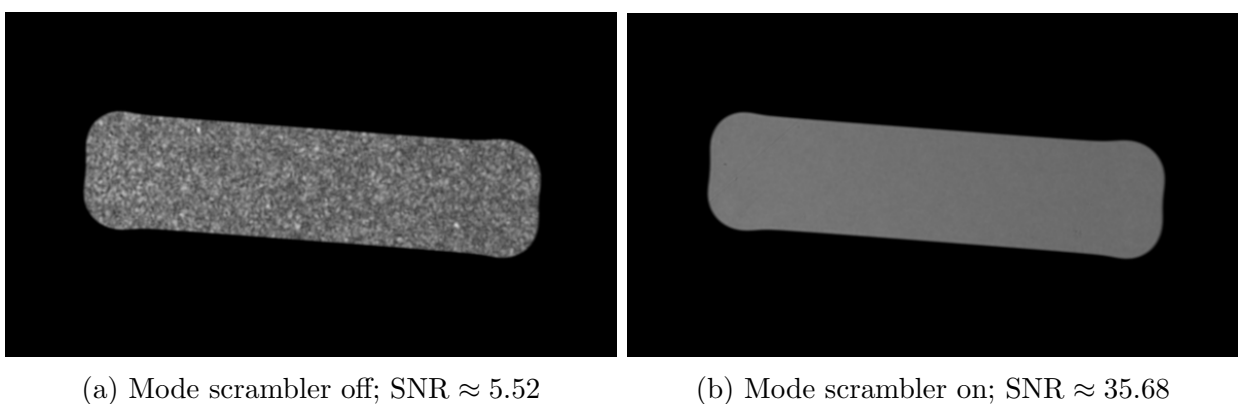


Figure 5.7: Near field images of a $400 \mu\text{m} \times 100 \mu\text{m}$ rectangular test fiber, with the mode scrambler was off (Figure 5.7a) and on (Figure 5.7b). Both images are a stack of 100 frames, with each individual frame having an exposure time of $350 \mu\text{s}$. Both images were acquired when the four-bar linkage-crank rocker was used, and bar *MA* was driven at 5 Hz.

5.4.2 Exposure Time and Number of Stacked Frames

The first set of experiments involved investigating the effects of exposure time and the number of stacked frames on scrambling. Suppose that a single image was taken when the mode scrambler was on. Intuitively, a single image with a longer exposure time should be more scrambled compared to one with a shorter exposure time, because the modal patterns change in time as the fiber is being agitated; hence the longer-exposed image should have more smoothed-out the modal patterns. This is a similar case for number of stacked frames. Suppose that a certain number of images were taken when the mode scrambler was on. Intuitively, if a larger number of these images are stacked together, then the stacked image would have more smoothed-out modal patterns, compared to a stacked image consisting of a smaller number of images stacked together. However, one cannot simply say that merely increasing the exposure time or number of stacked frames would constitute a mode scrambler. There should be some upper limit in both the exposure time and number of stacked frames, beyond which scrambling will only improve marginally (this limitation is due to the mode scrambler's inherent agitation performance). These quantities should be figured out before moving onto other experiments.

Three sets of data were taken in order to see the effect of exposure time and number of stacked frames on scrambling. This was done using the single rotating arm design (Section 4.2.1). In all of these three experiments, only one motor was used and the fiber was positioned at 7 inches away from the motor shaft. When the mode scrambler was on, the period and amplitude was held constant 2 s and 180° respectively. The test fiber was a 150 μm square fiber. The purpose of these tests is to inform us of what exposure time and number of stacked frames should be used moving forward in the other experiments.

5.4.2.1 Varying Number of Stacked Frames

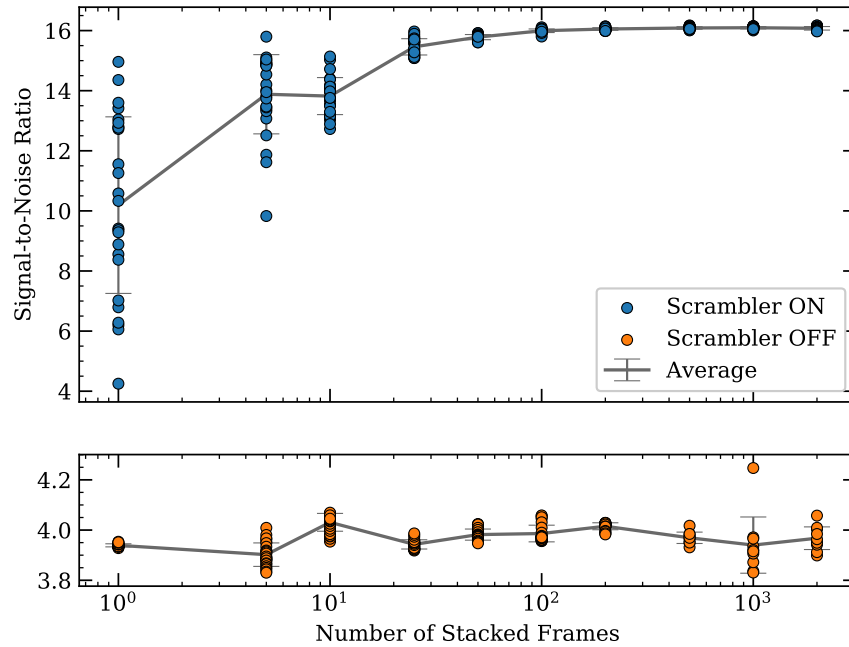


Figure 5.8: Plot of SNR versus number of stacked frames. Each individual frame had an exposure time of 750 μs . The test fiber used was a 150 μm square fiber.

In this experiment, the number of stacked frames was varied between 1 and 2000, while the exposure time of *individual* frames was held constant at 750 μs . The result is shown in Figure 5.8. In this figure, each data point represents a stacked image consisting of x frames, with each individual frame having an exposure time of 750 μs , where x is the value on the horizontal axis. The individual frames in each data point were acquired at 25 FPS. Dark correction was performed using 25 individual dark frames which were each taken with an exposure time of 750 μs .

In general, as the number of stacked frames increases, SNR also increases. However, there is a plateau in the data. The SNR values for $\gtrsim 100$ stacked frames are similar, which suggests that there is a certain point where increasing the number of stacked frames would not improve scrambling significantly.

5.4.2.2 Varying Exposure Time of Individual Frames

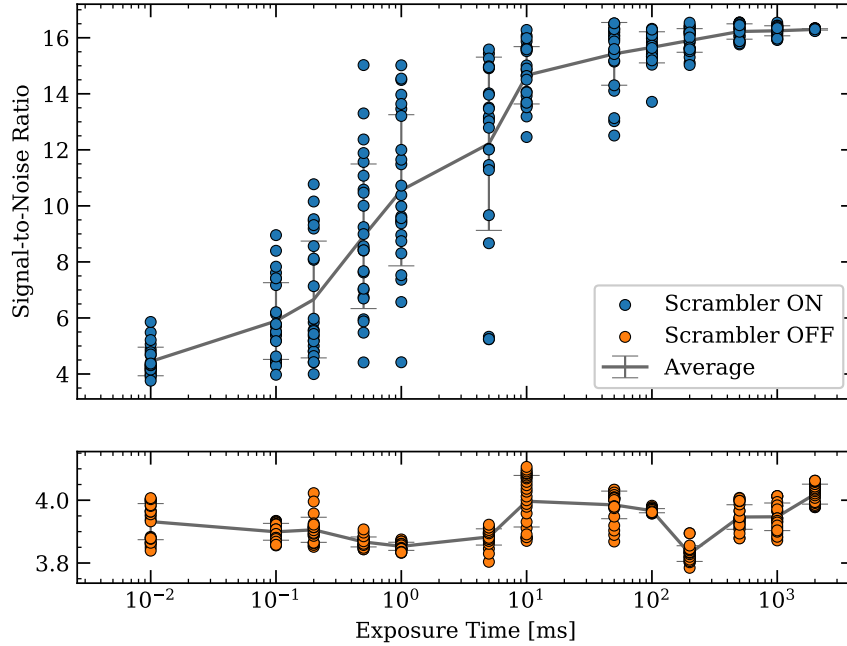


Figure 5.9: Plot of SNR versus exposure time for individual frames. The test fiber used was a $150\text{ }\mu\text{m}$ square fiber.

In this experiment, no frames were stacked, and the exposure time was varied between $10\text{ }\mu\text{s}$ (the minimum possible exposure time for the Matrix Vision mvBlueCOUGAR-XD camera) and 2 s . The result is shown in Figure 5.9. In this figure, each data point is an individual image with an exposure time of x , where x is the value on the horizontal axis. For each exposure time, 25 frames were acquired at a limiting frame rate of 25 FPS. Dark and bias corrections were performed. 5 dark frames were taken for each exposure time.

In general, as the exposure time increases, SNR also increases. However, the range of the average SNR values when varying exposure time (~ 4 to ~ 16 in Figure 5.9) appears to be greater than the range of the average SNR values when varying the number of stacked frames (~ 10 to ~ 16 in Figure 5.8), which suggests that perhaps exposure time has a more significant affect on SNR. In addition, there again appears to be a plateau in the data. There is not much difference in SNR between an exposure time of 0.5 s and 2 s .

5.4.2.3 Constant Total Exposure Time

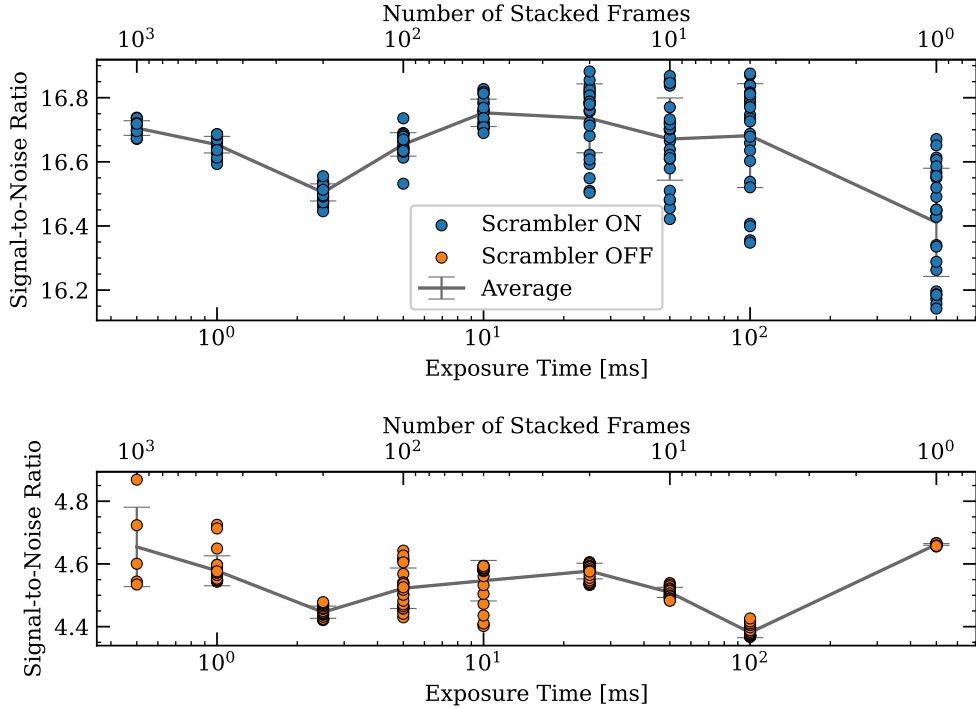


Figure 5.10: SNR for a constant total exposure time of 0.5 s, while varying individual frame exposure time and the number of stacked frames. The test fiber used was a 150 μm square fiber.

In this test, the total exposure time was held constant at 0.5 s, and the exposure times of individual frames and number of stacked frames were varied. That is, the product of the individual frame exposure time and the number of stacked frames was held constant. The result is shown in Figure 5.10. In this figure, each data point represents a stacked image consisting of x_{stack} frames, with each individual frame having an exposure time of $x_{t,\text{individual}}$, where x_{stack} and $x_{t,\text{individual}}$ are the values on the upper and lower horizontal axes respectively. Frames were acquired at a limiting frame rate of 25 FPS. Dark and bias corrections were performed. 20 dark frames were taken for each exposure time.

While keeping the total exposure time constant, the SNR did not change as significantly when compared to the previous two tests. Exposure time may have a more significant effect on scrambling than just stacking frames.

5.4.3 Shaft Distance

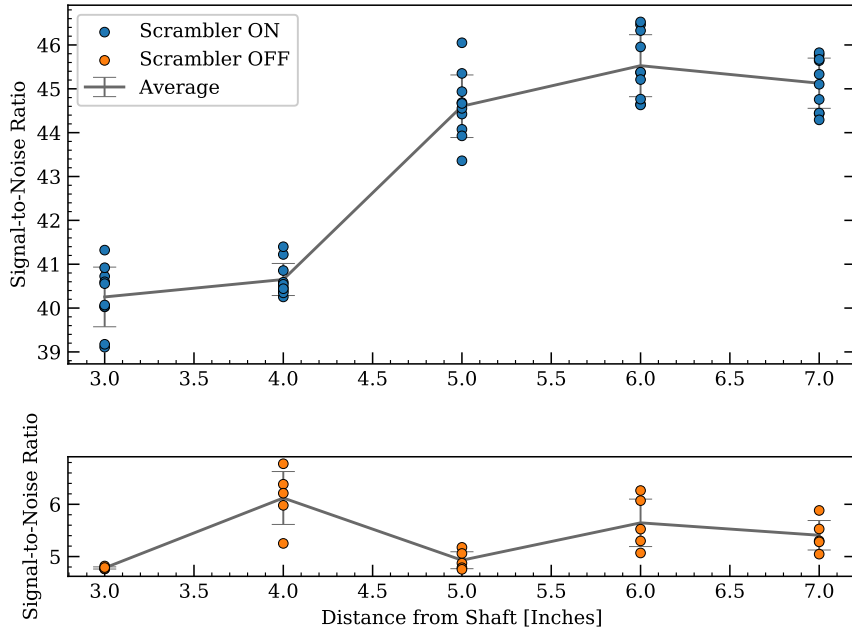


Figure 5.11: Plot of SNR versus distance away from shaft, for a freely-moving 400 μm by 100 μm rectangular fiber

In this experiment, the distance between the fiber and the motor shaft was varied between 3" and 7". The single rotating arm design was used, and the period and amplitude of the motor was held constant again at 2 s and 180° respectively. The result is shown in Figure 5.11. In this figure, each data point represents a stacked imaging consisting of 100 frames, with each individual frame having an exposure time of 650 μs . Dark, bias, and flat field corrections were applied to all images. A 400 μm by 100 μm rectangular fiber was used as a test fiber, and this fiber was free to move around (i.e. not clamped down to the table).

From the figure, one can see that for the most part, as the distance between the fiber and the motor shaft increases, the SNR also increases. The positive correlation between these two variables is intuitive because if the fiber is further away from the motor shaft, then it will move more and hence be agitated more. However, note that there appears to be some sort of plateau for distances beyond 6". It could be the case that if the distance is large, increasing it further would not make much of a difference on scrambling. More investigation is required.

5.4.4 Looping through Several Holes

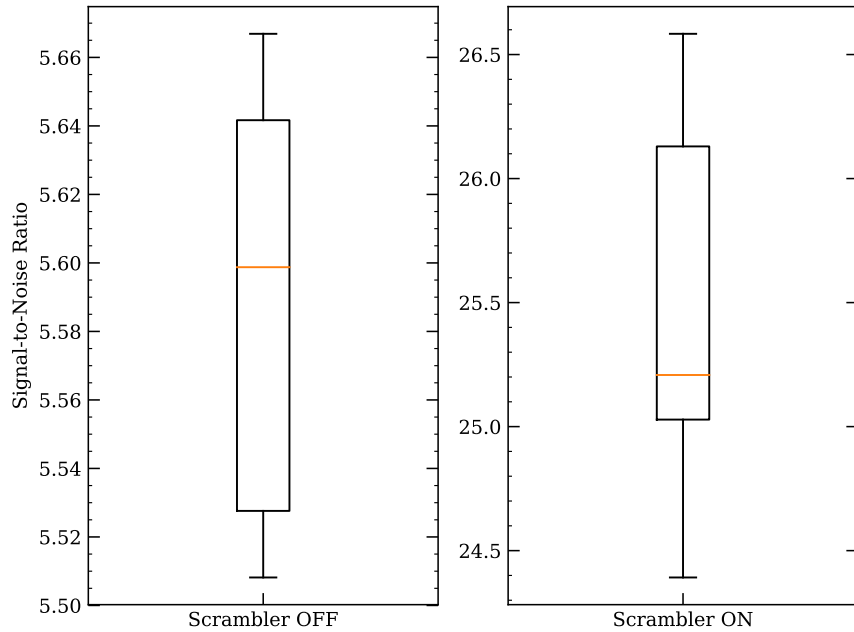


Figure 5.12: SNR for configuration where a test fiber is looped through several holes in the rotating arm. The test fiber used was a 400 μm by 100 μm rectangular fiber.

In this experiment, a rectangular fiber was looped/laced through all five holes in the single rotating arm. The period and amplitude of the motor was held constant again at 2 s and 180° respectively. The result is shown in the box-and-whisker plots in Figure 5.12. The left box-and-whisker plot contains data from 5 stacked frames, each consisting of 100 individual frames taken when the mode scrambler was off. The right box-and-whisker plot contains data from 20 stacked frames, each consisting of 100 individual frames taken when the mode scrambler was on. All of the individual frames had an exposure time of 500 μs .

From the figure, one can see that there is some scrambling going on when the mode scrambler is turned on. However, the SNR for when the mode scrambler is turned on here is less than that of in Figure 5.11, when the test fiber was just passed through one hole. One could say that for the rectangular fiber, not looping/lacing through all the holes is better than looping/lacing through all the holes. This is likely due to the high stiffness of the rectangular fiber. When the rectangular fiber is looped/laced through all the holes, the parts of the fiber between the holes cannot move too much (due to the fiber's stiffness) in comparison to when the fiber is passed through only one hole. There is less agitation when the fiber is looped/laced through all the holes.

5.4.5 Frequency

The final two experiments were conducted using the four-bar linkage crank-rocker design (Section 4.2.2). In these experiments, the motor frequency was varied. The four-bar linkage design is best suited for testing the effect of frequency on scrambling because the motor in this design will not slip at high frequencies, unlike the single rotating arm design. In both of the following experiments, the motor frequency was varied from 0.1 Hz to 3 Hz. Since there is a 40:24 gear ratio, the actual frequency of bar *MA* (see Figure 4.2) varies from ~ 0.17 Hz to 5 Hz. The frequency of bar *MA* is shown in the following plots.

5.4.5.1 Rectangular Fiber

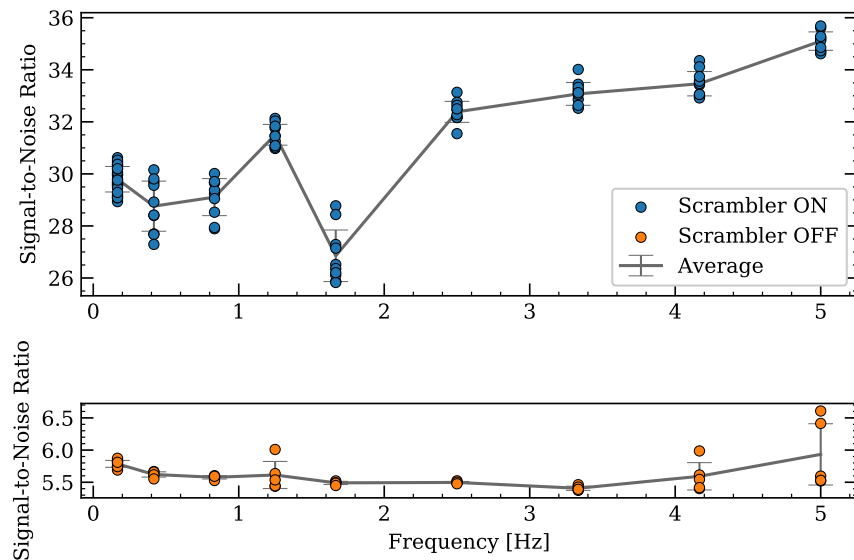


Figure 5.13: Plot of SNR versus frequency. Each data point represents 100 stacked frames, with each individual frame having an exposure time of 350 μ s. The test fiber used was a 400 μ m by 100 μ m rectangular fiber.

Figure 5.13 shows a plot of SNR versus frequency for a rectangular test fiber. Generally, as the frequency of the bar increases, the SNR also increases. The fiber is agitated more with higher frequencies, and hence there is better scrambling.

5.4.5.2 Octagonal Fiber

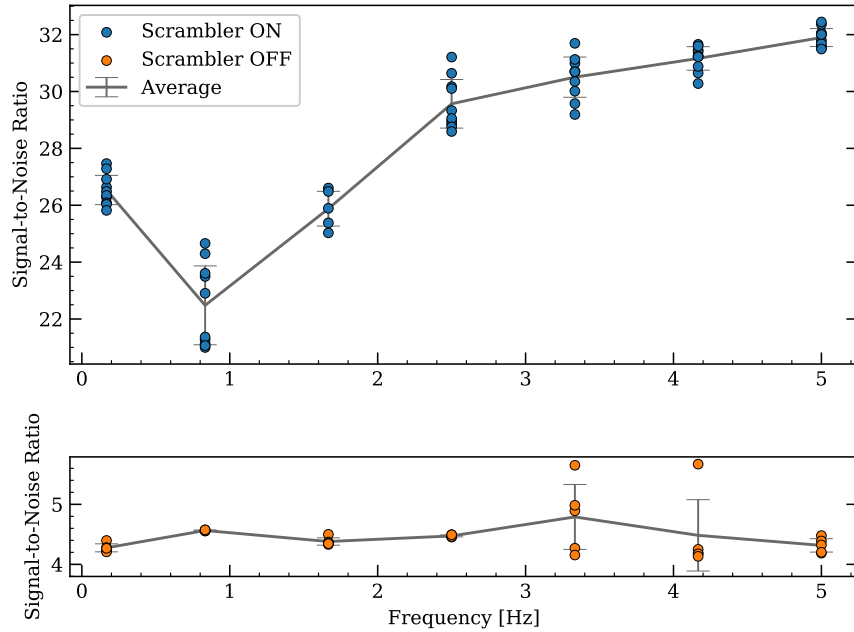


Figure 5.14: Plot of SNR versus frequency. Each data point represents 100 stacked frames, with each individual frame having an exposure time of 60 μ s. The test fiber used was a 100 μ m octagonal fiber.

Figure 5.14 shows a plot of SNR versus frequency for an octagonal test fiber. Like in Figure 5.13, as the frequency of the bar increases, the SNR also increases. In both Figures 5.13 and 5.14, it appears that the SNR will continue to increase with frequencies greater than 5 Hz. The motor was indeed able to be driven at higher frequencies, but the frequency of bar *MA* was limited to 5 Hz to avoid damage to the fibers. More investigation could be conducted into what the maximum frequency should be. Comparing Figures 5.14 and 5.13, the rectangular fiber appears to have slightly better mode scrambling than the octagonal fiber, but more investigation is required.

Chapter 6

Conclusion

6.1 Summary

The main conclusions of this project can be summarized as follows:

1. A Fiber Characterization Station (FCS) was redesigned and built at SAO CDP. The FCS allows for light to be injected into a test fiber, for images of the fiber near field, far field, and injection location to be acquired, and for fiber throughput and focal ratio degradation to be measured.
2. The FCS consists of two configurations (Sections 2.1.1 and 2.1.2) and four arms: one to inject light into a test fiber (pre-injection arm, Section 2.2), one to image the fiber injection position (injection imaging arm, Section 2.3), one to image the fiber near field (near field arm, Section 2.4), and one to image the fiber far field (far field arm, Section 2.5).
3. A variety of tools were used to align the FCS (Chapter 3). Custom software was developed to control the cameras and to provide GUIs for aid in alignment (Section 3.4).
4. All of the arms, with the exception of the far field arm, were aligned successfully. The OAP in the far field arm caused numerous problems in alignment, and another solution has been suggested (Section 3.3.4).
5. A prototype mode scrambler was designed and built, consisting of two stepper motors that move simultaneously at different periods and amplitudes to agitate a fiber.
6. Two different mechanical designs were used and tested for the prototype mode scrambler: a single rotating arm (Section 4.2.1), and a four-bar linkage crank-rocker (Section

- 4.2.2). The four-bar linkage crank-rocker was more reliable than the simple rotating arm and did not slip.
7. The mode scrambler is controlled by an Arduino, with all electronic components put into an easy-to-access electronics box (Section 4.3). Both mechanical designs use the same electronics.
 8. Custom software was developed to reliably identify the boundary of the face of a fiber in a near field image. Alpha shapes was a novel approach that was used (Section 5.3.2.2).
 9. For the mode scrambler experiments, increasing the exposure time and number of stacked frames increases SNR, but only up to a certain point (Section 5.4.2).
 10. For the mode scrambler experiments, increasing the distance between the test fiber and the motor shaft increases SNR. For larger distances, perhaps the effect becomes negligible (Section 5.4.3).
 11. Looping/lacing a rectangular fiber through all holes of the single rotating arm makes the scrambling performance worse than if the fiber just passes through one hole (Section 5.4.4).
 12. For the mode scrambler experiments, increasing the motor frequency increases SNR (Section 5.4.5). The rectangular fiber appears to have slightly better mode scrambling than the octagonal fiber when looking at the effect of motor frequency on SNR, but more investigation is required.

6.2 Next Steps

The work in this project has laid a strong foundation for future investigations into mode scrambling. The FCS was built and successfully aligned (with the exception of the far field arm), two prototype designs for the mode scrambler were completed, and custom software was developed for FCS alignment, mode scrambler control, image acquisition, and image analysis. With these, more further scrambling experiments could be conducted. One next step of this project would be to replace the OAP in the far field arm with a flat mirror and a 100 mm EFL lens, since the OAP has been causing alignment issues.

Another next step would be to conduct more experiments using the four-bar linkage crank-rocker design. This design was only conceived near the end of this project, and due to

CHAPTER 6. CONCLUSION

time constraints, only the effect of motor frequency on scrambling was investigated using this design. However, from only a few tests, it was observed that the performance and reliability of this design is much better than that of the single rotating arm. Perhaps other parameters such as shaft distance and bar amplitude could be investigated using the four-bar linkage crank-rocker (with simple modifications to the bar lengths). The motor in the single rotating arm design frequently slipped due to a lack of torque, preventing further investigations into cases where the shaft distance was greater than 7"; this could be investigated using the four-bar linkage crank-rocker design instead. In addition, a wider variety of types of fibers could also be investigated.

Furthermore, with the mode scrambler control software, image acquisition and analysis software, and mode scrambler electronics and hardware, more different mechanical designs could be prototyped and investigated. The current software and hardware was designed so that different mechanical designs would also be compatible. Another next step would be to investigate the effect of using multiple motors to agitate the fiber. The current designs allow for this, but this was not investigated thoroughly due to time constraints. Once a suitable mechanical design has been decided, the next step would be to move from prototyping to production.

Bibliography

- Akinlar, C., & Chome, E. 2016, Journal of Visual Communication and Image Representation, 36, 159, doi: [10.1016/j.jvcir.2016.01.017](https://doi.org/10.1016/j.jvcir.2016.01.017)
- Avila, G., Singh, P., & Albertsen, M. 2006, in Proc. SPIE, Vol. 6269, Ground-based and Airborne Instrumentation for Astronomy, 62695O, doi: [10.1117/12.671417](https://doi.org/10.1117/12.671417)
- Dhillon, D., & Chouhan, R. 2022, IEEE Access, 10, 11191, doi: [10.1109/access.2022.3145428](https://doi.org/10.1109/access.2022.3145428)
- Edelsbrunner, H., & Mücke, E. P. 1994, ACM Trans. Graph., 13, 43–72, doi: [10.1145/174462.156635](https://doi.org/10.1145/174462.156635)
- Fischer, D. A., Anglada-Escude, G., Arriagada, P., et al. 2016, Publications of the Astronomical Society of the Pacific, 128, 066001, doi: [10.1088/1538-3873/128/964/066001](https://doi.org/10.1088/1538-3873/128/964/066001)
- Fischer, K. 2000, Introduction to Alpha Shapes, https://graphics.stanford.edu/courses/cs268-11-spring/handouts/AlphaShapes/as_fisher.pdf
- Frank, C., Kerber, F., Avila, G., et al. 2018, in Proc. SPIE, Vol. 10702, Ground-based and Airborne Instrumentation for Astronomy VII, 107026P, doi: [10.1117/12.2313484](https://doi.org/10.1117/12.2313484)
- Gardiner, J. D., Behnson, J., & Brassey, C. A. 2018, BMC Evolutionary Biology, 18, doi: [10.1186/s12862-018-1305-z](https://doi.org/10.1186/s12862-018-1305-z)
- Halverson, S., Roy, A., Mahadevan, S., et al. 2015, The Astrophysical Journal, 806, 61, doi: [10.1088/0004-637x/806/1/61](https://doi.org/10.1088/0004-637x/806/1/61)
- Ishizuka, M., Kotani, T., Nishikawa, J., et al. 2018, Publications of the Astronomical Society of the Pacific, 130, 065003, doi: [10.1088/1538-3873/aab8d0](https://doi.org/10.1088/1538-3873/aab8d0)
- Petersburg, R. R., McCracken, T. M., Eggerman, D., et al. 2018, The Astrophysical Journal, 853, 181, doi: [10.3847/1538-4357/aaa487](https://doi.org/10.3847/1538-4357/aaa487)

BIBLIOGRAPHY

Sablowski, D. P., Plüsckke, D., Weber, M., Strassmeier, K. G., & Järvinen, A. 2016, Astronomische Nachrichten, 337, 216, doi: [10.1002/asna.201412299](https://doi.org/10.1002/asna.201412299)

Sirk, M. M., Wishnow, E. H., Weisfeiler, M., et al. 2018, in Proc. SPIE, Vol. 10702, Ground-based and Airborne Instrumentation for Astronomy VII, 107026F, doi: [10.1117/12.2312945](https://doi.org/10.1117/12.2312945)

Szentgyorgyi, A., Baldwin, D., Barnes, S., et al. 2018, in Proc. SPIE, Vol. 10702, Ground-based and Airborne Instrumentation for Astronomy VII, 107021R, doi: [10.1117/12.2313539](https://doi.org/10.1117/12.2313539)

Tuttle, S., Farr, E., Poppett, C., et al. 2020, in Proc. SPIE, Vol. 11447, Ground-based and Airborne Instrumentation for Astronomy VIII, 114478T, doi: [10.1117/12.2562293](https://doi.org/10.1117/12.2562293)